



Lie groups-based SINS/GNSS algorithm for guided projectiles in launch-centered earth-fixed frame under large misalignment

Kai Chen^{a,*}, Chengzhi Zeng^a, Peng Huang^b, Zhenhao Li^a, Jiang He^c

^a School of Astronautics, Northwestern Polytechnical University, Xi'an 710072, China

^b Northwest Industries Group Corporation, Xi'an 710043, China

^c AVIC Xi'an Flight Automatic Control Research Institute, Xi'an 710000, China

ARTICLE INFO

Editor: Dr. Xingqun Zhan

Keywords:

Guided projectile
Launch-centered earth-fixed frame
Integrated navigation
Lie groups
Large misalignment

ABSTRACT

Traditional integrated navigation algorithms for guided projectiles face significant roll error resulting from poor MEMS IMU accuracy and limited observability of roll angles during in-flight alignment. This article introduces a Lie groups-based Kalman filter (LG-KF) SINS/GNSS algorithm in the launch-centered earth-fixed (LCEF) frame to enhance navigation convergence and accuracy under conditions of large misalignment and poor IMU performance. First, a Lie group-based mechanization model for guided projectile is established to provide a foundation for SINS error model. Then, the LG-KF integrated navigation algorithm in the LCEF frame is designed, demonstrating inherent nonlinearity error reduction in principle. Subsequently, simulation experiments and a road test are conducted to compare the LG-KF algorithm with EKF, ST-EKF, and Quat-EKF. The results indicate that LG-KF effectively mitigates nonlinear errors associated with large misalignments in integrated navigation, exhibiting higher convergence speed and accuracy compared to the other three algorithms. LG-KF stands out as the sole algorithm among the four to achieve convergence with roll misalignment error of $\pm 140^\circ$.

1. Introduction

Hypervelocity projectiles (HVPs) experience shocks of 10,000 to 30,000g (g as the unit of acceleration, where $1g = 9.81 \text{ m/s}^2$) and high-speed spinning with the initial launch [1]. The shocks and spinning exceeds the measurement ranges of inertial measurement unit (IMU), preventing the strapdown inertial navigation system (SINS) work during launch. In fact, most of guided projectiles estimate its attitude, velocity and position after launch, and the estimation of attitude is called in-flight alignment. The error of attitude estimation, also known as misalignment, is typically large because of the limited navigation information and significant IMU errors. Large misalignment is a challenge for the integrated navigation. Substantial deviations between initial navigation states and true physical conditions can trigger mismatch between empirical and theoretical covariance, severely compromising system stability [2,3].

After launch, projectiles activate thermoelectric batteries, complicating in-flight alignment when the movement of HVP is almost free-fall. The position and velocity can be observed in relatively high accuracy by

Global Navigation Satellite System (GNSS), the attitude, however, is not observable, and the uncertainty of attitude will make the SINS work in a wrong state.

Numerous in-flight alignment methodologies have been developed specifically to address the attitude estimation challenge in HVPs. A functional iteration in-flight alignment method proposed by Wang integrated the information of MSINS and GNSS by Legendre polynomials [4]. However, the attitude error deteriorates scenarios demanding shorter alignment times in near-boundary with only several second for alignment. Li proposed an air coarse alignment method based on kinematics constraints to estimate the roll angle [5]. But the accuracy of this method may be deteriorated by aerodynamic, structural asymmetries, servo deadband errors of electrical or mechanical of HVPs. Guided projectiles experience significant challenges in integrated navigation with large misalignment angles, posing adaptation difficulties for current navigation algorithm.

Although a considerable number of in-flight alignment methods for HPV are proposed, large misalignment still remains a problem for HVP navigation. Firstly, Gyro bias errors can reach several degrees per

This work is supported by the National Natural Science Foundation of China (62373303).

* Corresponding author.

E-mail addresses: npuck@nwpu.edu.cn (K. Chen), zeng_zc@mail.nwpu.edu.cn (C. Zeng), huangpeng0805@126.com (P. Huang), lizhenhao@mail.nwpu.edu.cn (Z. Li), 389741542@qq.com (J. He).

<https://doi.org/10.1016/j.ast.2025.110239>

Received 25 December 2024; Received in revised form 17 March 2025; Accepted 21 April 2025

Available online 15 May 2025

1270-9638/© 2025 Elsevier Masson SAS. All rights reserved, including those for text and data mining, AI training, and similar technologies.

second, and accelerometer drift can reach several milli *g* after high-*g* shocks. The degradation of IMU accuracy under high-*g* shocks compromises projectile in-flight alignment precision. Secondly, roll angle estimation requires the practical trajectory adhere to the design, thus alignment accuracy can be degraded by aerodynamic-structural asymmetries and servo mechanism nonlinearities in HVPs.

Extensive research has been conducted to eliminate linearization errors associated with large misalignment angles nonlinearity. Wang established an error model of SINS and introduced a Lyapunov equivalent transformation to derive the equivalence of SINS and gimballed inertial navigation system (GINS). An integrated navigation Kalman filter based on this transformation was then designed and used to estimate IMU errors, though all discussions are ground-based [6]. Li designed a robust adaptive SINS/CNS integrated navigation (RASCIN) based on the traditional EKF to mitigate the influence of observation errors in celestial measurements by adjusting the weight matrix. The attitude solution of RASCIN converge with yaw misalignment of 15° [7].

Wang proposed a state transformation extended Kalman filter (ST-EKF) for GPS/SINS tightly coupled integration to adapt the filter to head misalignment of 20° [8]. Lu proposed a backward smooth singular value decomposition cubature Kalman filter (SVDCKF) algorithm,[9] achieving integrated navigation under large misalignment angles. However, unscented Kalman filter (UKF) and CKF are nonlinear algorithms based on sigma points, whose performance depends on the selection of sigma points in nonlinear systems. Particle filtering (PF), suitable for strong nonlinearity, was introduced by Hao as an integrated navigation algorithm,[10] estimating attitude during in-motion alignment, with misalignment angles of [10°, 10°, 60°] (60° in head). However, PF requires a substantially larger number of particles (hundreds of times more than the sigma points of UKF and CKF), resulting in considerably higher computational burdens compared to UKF and CKF.

The SINS is inherently nonlinear. Traditional algorithms linearize the SINS, adopting small disturbance hypothesis, which is unsuitable for large misalignment navigation [11]. Therefore, a method that can describe rotations linearly and a system model that remains linear even under large misalignment angles must be established to mathematically address the linearization errors associated with large misalignment angles. Barrau introduced a Lie groups error model for inertial systems, including left and right error models, and described attitude error models in the special Euclidean (SE) group [12]. Barrau also proposed a probabilistic approach for intrinsic filtering of a system on a matrix Lie groups with invariance properties [13]. Chang proposed a log-linear model, highlighting that the affine properties of Lie groups make the error models applicable to arbitrary misalignment, which is highly advantageous for integrated navigation dealing with large misalignment [14]. Tang indicated that Lie groups-based state-space models can be considered linear error models, designing an integrated SINS/DVL navigation system for underwater applications that improved heading and horizontal attitude convergence speed and precision under misalignment of [10°, 10°, 120°] (120° in heading). Tang also suggested the potential of this algorithm for integrating the alignment and navigation [15]. Xu established the SE(2) model for in-motion alignment of shipborne carriers [16].

Considering the guidance and control requirements of HVPs, this study selects the launch-centered Earth-fixed (LCEF) frame as the navigation frame, which is defined as Table 1 [17].

Table 1
Definition of LCEF frame.

Reference Frame	launch-centered Earth-fixed, non-inertial
Origin	Projectile launch point
X-axis	Target direction (azimuth)
Y-axis	Right-handed completion
Z-axis	Local vertical (upwards)
Handedness	Right-hand rule (ENU)

The advantages of strapdown inertial navigation in the LCEF frame have been discussed in previous work[18–21]. In the attitude equation for the LCEF frame, the attitude solution depends solely on the initial attitude value and gyroscope output, avoiding the influence of accelerometer errors on the attitude calculation [18]. In the specific force equation of the LCEF frame, the Coriolis acceleration term is constant, with its derivative being a zero matrix [19,20]. The LCEF frame strapdown algorithm can compensate for non-commutativity errors, achieving an error-free strapdown algorithm [21].

Since Barrau made the first attempt to design filters on SO(3),[22] Lie groups theory has been used in integrated navigation system of different vehicles, such as aircrafts and UAVs [14,15]. The potential application of LG-KF is rather attractive. Li group based integrated navigation algorithm outperformed traditional algorithms in handling with large misalignment. Navigation results will keep reliable even when the alignment fails, as the performance of navigation algorithm is enhanced.

This study presents a novel Lie groups-based Kalman filter (LG-KF) method integrated in the LCEF frame, which addresses challenges posed by large misalignment in guided projectiles' navigation systems. The proposed method ensures navigation system convergence under large misalignment, relaxes the precision requirements for in-flight alignment of guided projectiles, and reduces the response time. First, we designed the LG-KF based on SE(3) left error model before analyzing error propagation. Then the filtering process model in the LCEF frame is proved to be independent of state estimates, which is highly advantageous when initial alignment errors are large in SINS. Subsequently, simulations and road test are conducted to prove the advantage of LG-KF.

Section 2 discusses the description of the navigation state in the LCEF frame under a special Euclidean group and the navigation algorithm in the LCEF frame. Section 3 introduces the of LG error model in LCEF. Section 4 elaborates on the design of the Lie groups integrated navigation algorithm in the LCEF frame, including error models, state equation, measurement equation, and integrated navigation algorithms. Section 5 demonstrates the navigation simulation and a road test results, four algorithms are analyzed and compared, verifying the convergence and accuracy advantages of LG-KF in integrated navigation under large misalignment angles. The conclusions are presented in Section 6.

2. LG-KF integrated navigation algorithm in the LCEF frame

2.1. Lie groups and Lie algebra

A group is an algebraic structure satisfying closure, associativity, identity element, and invertibility properties under a binary operation. Lie groups, which are differential manifolds with smooth or differentiable group operations, include general linear groups, special orthogonal groups, and special Euclidean groups. These groups naturally combine algebraic and geometric structures through differential manifolds, making them suitable for solving differential equation problems in navigation.

The special orthogonal (SO) group and the special Euclidean (SE) group, formed respectively by matrix multiplication with sets of rotation matrices and transformation matrices, are primarily used to describe rigid body motion. This section provides useful matrix Lie groups formulas to derive corresponding error models.

Carrier motion can be viewed as one coordinate system transforming into another through attitude rotation and position/velocity translation. Rotation is described by a 3×3 matrix \mathbf{R} , and velocity/position translation by three-dimensional vectors \mathbf{V} and \mathbf{P} , denoted as SO(3) and SE(3), respectively.

$$\begin{cases} SO(3) = \{ \mathbf{R} \in SO(3) | \mathbf{R}\mathbf{R}^T = \mathbf{I}_{3 \times 3}, \det \mathbf{R} = 1 \} \\ SE_2(3) = \left\{ \mathbf{T} = \begin{bmatrix} \mathbf{R} & \mathbf{V} & \mathbf{P} \\ \mathbf{0}_{1 \times 3} & 1 & 0 \\ \mathbf{0}_{1 \times 3} & 0 & 1 \end{bmatrix} \in \mathbb{R}^{5 \times 5} \mid \mathbf{R} \in SO(3), \mathbf{V}, \mathbf{P} \in \mathbb{R}^3 \right\} \end{cases} \quad (1)$$

The Lie algebra associated with $SO(3)$ and $SE(3)$ are represented by $so(3)$ and $se_2(3)$:

$$\begin{cases} so(3) = \{ \boldsymbol{\theta} | \boldsymbol{\theta} \in \mathbb{R}^3, [\boldsymbol{\theta} \times] \in \mathbb{R}^{3 \times 3} \} \\ se_2(3) = \left\{ \boldsymbol{\zeta} = \begin{bmatrix} \boldsymbol{\theta} \\ \mathbf{v} \\ \boldsymbol{\rho} \end{bmatrix} \mid \boldsymbol{\theta} \in so(3), \mathbf{v}, \boldsymbol{\rho} \in \mathbb{R}^3, \hat{\boldsymbol{\zeta}} = \begin{bmatrix} \boldsymbol{\theta} \times & \mathbf{v} & \boldsymbol{\rho} \\ \mathbf{0}_{1 \times 3} & 0 & 0 \\ \mathbf{0}_{1 \times 3} & 0 & 0 \end{bmatrix} \in \mathbb{R}^{5 \times 5} \right\} \end{cases} \quad (2)$$

where $\boldsymbol{\theta}$ represents a three-dimensional rotation vector, \mathbf{v} and $\boldsymbol{\rho}$ denote three-dimensional translation vectors.

A Lie groups $SO(3)$, $SE(3)$ and its associated Lie algebra $so(3)$ and $se_2(3)$ are linked through the exponential map:

$$\begin{aligned} \mathbf{R} &= \exp(\boldsymbol{\theta} \times) = \exp(\boldsymbol{\theta} \mathbf{a} \times) \\ &= \cos \theta \mathbf{I}_{3 \times 3} + (1 - \cos \theta) \mathbf{a} \mathbf{a}^T + \sin \theta (\mathbf{a} \times) \\ \mathbf{T} = \exp(\hat{\boldsymbol{\zeta}}) &= \begin{bmatrix} \exp(\boldsymbol{\theta} \times) & \mathbf{J} \mathbf{v} & \mathbf{J} \boldsymbol{\rho} \\ \mathbf{0}_{1 \times 3} & 1 & 0 \\ \mathbf{0}_{1 \times 3} & 0 & 1 \end{bmatrix} \end{aligned} \quad (3)$$

where $\theta = |\boldsymbol{\theta}|$, \mathbf{a} represents the unit vector of $\boldsymbol{\theta}$, \exp represents the exponential mapping of matrices, \mathbf{v} and $\boldsymbol{\rho}$ represent 3D translation vectors, and \mathbf{J} represents the Jacobian matrix of $SO(3)$.

$$\mathbf{J} = \frac{\sin \theta}{\theta} \mathbf{I}_{3 \times 3} + \left(1 - \frac{\sin \theta}{\theta}\right) \mathbf{a} \mathbf{a}^T + \left(\frac{1 - \cos \theta}{\theta}\right) [\mathbf{a} \times] \quad (4)$$

The inverse of $SE(3)$ can be given as follows:

$$\mathbf{T}^{-1} = \begin{bmatrix} \mathbf{R} & -\mathbf{R}^T \mathbf{V} & -\mathbf{R}^T \mathbf{P} \\ \mathbf{0}_{1 \times 3} & 1 & 0 \\ \mathbf{0}_{1 \times 3} & 0 & 1 \end{bmatrix} \in SE_2(3) \quad (5)$$

In a LCEF frame, the position velocity and attitude are loose coupled, and the affine properties of the Lie groups are satisfied. Thus, selecting the LCEF frame enables the navigation error to extend straightforwardly to the SE group, eliminating the nonlinearity of attitude error.

2.2. Lie groups-based mechanization in the LCEF frame

The strapdown inertial navigation mechanization in the LCEF frame is represented as follows:¹⁹

$$\begin{bmatrix} \dot{\mathbf{P}}^g \\ \dot{\mathbf{V}}^g \\ \dot{\mathbf{R}}_b^g \end{bmatrix} = \begin{bmatrix} \mathbf{V}^g \\ \mathbf{R}_b^g \mathbf{f}^b - 2\boldsymbol{\Omega}_{ag}^g \mathbf{V}^g + \mathbf{g}^g \\ \mathbf{R}_b^g \boldsymbol{\Omega}_{gb}^b \end{bmatrix} \quad (6)$$

where \mathbf{P}^g and \mathbf{V}^g denote the position and velocity vectors of the carrier in the LCEF frame (also marked as g -frame). \mathbf{R}_b^g represents the carrier's attitude matrix in the g -frame. \mathbf{f}^b denotes the specific force measured by the accelerometer. $\boldsymbol{\Omega}_{ag}^g$ is the skew-symmetric matrix of the rotation angular velocity $\boldsymbol{\omega}_{ag}^g$ of the LCEF frame relative to the launch-centered inertial frame (also marked as a -frame). \mathbf{g}^g is the gravity vector in the

LCEF frame. $\boldsymbol{\Omega}_{gb}^b$ is the skew-symmetric matrix of the rotation angular velocity $\boldsymbol{\omega}_{gb}^b$ of the body frame (also marked as b -frame) relative to the LCEF frame.

$$\boldsymbol{\Omega}_{gb}^b = \boldsymbol{\Omega}_{ab}^b - \boldsymbol{\Omega}_{ag}^g \quad (7)$$

where $\boldsymbol{\Omega}_{ab}^b$ represents the skew-symmetric matrix of angular velocity measured by gyroscope, $\boldsymbol{\Omega}_{ig}^b = \mathbf{R}_g^b \boldsymbol{\Omega}_{ig}^g \mathbf{R}_b^g$.

The relationship for gravity \mathbf{g}^g in the LCEF frame can be expressed as follows:

$$\mathbf{g}^g = \mathbf{G}^g - \boldsymbol{\Omega}_{ag}^g \boldsymbol{\Omega}_{ag}^g \mathbf{P}^g \quad (8)$$

where \mathbf{G}^g represents gravitation at \mathbf{P}^g .

The auxiliary velocity vector $\bar{\mathbf{V}}^g$ in the LCEF frame is constructed as follows:

$$\bar{\mathbf{V}}^g = \mathbf{V}^g + \boldsymbol{\Omega}_{ag}^g \mathbf{P}^g \quad (9)$$

Using the constructed auxiliary velocity vector, the strapdown inertial navigation differential equations in the LCEF frame are given as follows:

$$\begin{bmatrix} \dot{\mathbf{P}}^g \\ \dot{\bar{\mathbf{V}}}^g \\ \dot{\mathbf{R}}_b^g \end{bmatrix} = \begin{bmatrix} \bar{\mathbf{V}}^g - \boldsymbol{\Omega}_{ag}^g \mathbf{P}^g \\ \mathbf{R}_b^g \mathbf{f}^b - \boldsymbol{\Omega}_{ag}^g \bar{\mathbf{V}}^g + \mathbf{G}^g \\ \mathbf{R}_b^g \boldsymbol{\Omega}_{gb}^b \end{bmatrix} \quad (10)$$

Incorporating the attitude rotation matrix \mathbf{R}_b^g , velocity $\bar{\mathbf{V}}^g$, and position \mathbf{P}^g into the Lie groups, the Lie groups state variables can be constructed as follows:

$$\boldsymbol{\chi} = \begin{bmatrix} \mathbf{R}_b^g & \bar{\mathbf{V}}^g & \mathbf{P}^g \\ \mathbf{0}_{1 \times 3} & 1 & 0 \\ \mathbf{0}_{1 \times 3} & 0 & 1 \end{bmatrix} \in SE_2(3) \quad (11)$$

Therefore, the strapdown inertial navigation differential equations in the LCEF frame can be rewritten as a dynamic model:

$$\dot{\boldsymbol{\chi}} = f(\boldsymbol{\chi}) = \begin{bmatrix} \mathbf{R}_b^g \boldsymbol{\Omega}_{gb}^b & \mathbf{R}_b^g \mathbf{f}^b - \boldsymbol{\Omega}_{ag}^g \bar{\mathbf{V}}^g + \mathbf{G}^g & \bar{\mathbf{V}}^g - \boldsymbol{\Omega}_{ag}^g \mathbf{P}^g \\ \mathbf{0}_{1 \times 3} & 1 & 0 \\ \mathbf{0}_{1 \times 3} & 0 & 1 \end{bmatrix} \quad (12)$$

3. Lie groups based nonlinear error state model in the LCEF frame

3.1. Lie groups-based error model

According to the definition of state error, Lie groups error models can be classified into left error model τ_l and right error model τ_r .

$$\begin{cases} \tau_l = \tilde{\boldsymbol{\chi}}^{-1} \boldsymbol{\chi}_1 \\ \tau_r = \boldsymbol{\chi} \tilde{\boldsymbol{\chi}} \end{cases} \quad (13)$$

The state variables of the Lie groups are inverted as follows:

$$\boldsymbol{\chi}^{-1} = \begin{bmatrix} \mathbf{R}_b^g & -\mathbf{R}_b^g \bar{\mathbf{V}}^g & -\mathbf{R}_b^g \mathbf{P}^g \\ \mathbf{0}_{1 \times 3} & 1 & 0 \\ \mathbf{0}_{1 \times 3} & 0 & 1 \end{bmatrix} \in SE_2(3) \quad (14)$$

3.1.1. Lie groups right error model in the LCEF frame

By combining equations (11), (13), and (14), the transmission system Lie groups SINS right error model is derived as follows:

$$\begin{aligned} \tau_r = \tilde{\chi} \tilde{\chi}^{-1} &= \begin{bmatrix} \mathbf{R}_b^g & \bar{\mathbf{V}}^g & \mathbf{P}^g \\ \mathbf{0}_{1 \times 3} & 1 & 0 \\ \mathbf{0}_{1 \times 3} & 0 & 1 \end{bmatrix} \begin{bmatrix} \tilde{\mathbf{R}}_g^b & -\tilde{\mathbf{R}}_g^b \tilde{\mathbf{V}}^g & -\tilde{\mathbf{R}}_g^b \tilde{\mathbf{P}}^g \\ \mathbf{0}_{1 \times 3} & 1 & 0 \\ \mathbf{0}_{1 \times 3} & 0 & 1 \end{bmatrix} \\ &= \begin{bmatrix} \mathbf{R}_b^g \tilde{\mathbf{R}}_g^b & \bar{\mathbf{V}}^g - \mathbf{R}_b^g \tilde{\mathbf{R}}_g^b \tilde{\mathbf{V}}^g & \mathbf{P}^g - \mathbf{R}_b^g \tilde{\mathbf{R}}_g^b \tilde{\mathbf{P}}^g \\ \mathbf{0}_{1 \times 3} & 1 & 0 \\ \mathbf{0}_{1 \times 3} & 0 & 1 \end{bmatrix} = \begin{bmatrix} \tau_r^a & \tau_r^v & \tau_r^p \\ \mathbf{0}_{1 \times 3} & 1 & 0 \\ \mathbf{0}_{1 \times 3} & 0 & 1 \end{bmatrix} \in SE(3) \end{aligned} \quad (15)$$

where, $\tilde{\mathbf{R}}_g^b$, $\tilde{\mathbf{V}}^g$ and $\tilde{\mathbf{P}}^g$ represent the navigation parameters calculated by the inertial navigation system. \mathbf{R}_b^g , $\bar{\mathbf{V}}^g$, and \mathbf{P}^g denote the true navigation parameters. τ_r^a , τ_r^v , and τ_r^p are the attitude, velocity, and position errors defined on right error model of Lie groups in the LCEF frame.

Let ϕ_r denote the misalignment angle error of the right error model, with its skew-symmetric matrix as ψ_r ($\psi_r = [\phi_r \times]$). When ϕ_r is minimized, τ_r^a can be derived based on the relationship between Lie groups and Lie algebra:

$$\tau_r^a = \mathbf{R}_b^g \tilde{\mathbf{R}}_g^b = \exp(\phi_r \times) \approx \mathbf{I}_{3 \times 3} + \phi_r \times \quad (16)$$

Using this equation, corresponding velocity and position error vectors for the right error model can be deduced as follows:

$$\tau_r^v = \bar{\mathbf{V}}^g - \mathbf{R}_b^g \tilde{\mathbf{R}}_g^b \tilde{\mathbf{V}}^g = -\delta \bar{\mathbf{V}}^g + (\tilde{\mathbf{V}}^g \times) \phi_l \quad (17)$$

$$\tau_r^p = \mathbf{P}^g - \mathbf{R}_b^g \tilde{\mathbf{R}}_g^b \tilde{\mathbf{P}}^g = -\delta \mathbf{P}^g + (\tilde{\mathbf{P}}^g \times) \phi_l \quad (18)$$

where $\delta \bar{\mathbf{V}}^g = \tilde{\mathbf{V}}^g - \bar{\mathbf{V}}^g$ and $\delta \mathbf{P}^g = \tilde{\mathbf{P}}^g - \mathbf{P}^g$.

3.1.2. Lie groups left error model in the LCEF frame

By combining equations (11), (13), and (14), the transmission system Lie groups SINS left error model is derived as follows:

$$\begin{aligned} \tau_l = \tilde{\chi}^{-1} \chi &= \begin{bmatrix} \tilde{\mathbf{R}}_g^b & -\tilde{\mathbf{R}}_g^b \tilde{\mathbf{V}}^g & -\tilde{\mathbf{R}}_g^b \tilde{\mathbf{P}}^g \\ \mathbf{0}_{1 \times 3} & 1 & 0 \\ \mathbf{0}_{1 \times 3} & 0 & 1 \end{bmatrix} \begin{bmatrix} \mathbf{R}_b^g & \bar{\mathbf{V}}^g & \mathbf{P}^g \\ \mathbf{0}_{1 \times 3} & 1 & 0 \\ \mathbf{0}_{1 \times 3} & 0 & 1 \end{bmatrix} \\ &= \begin{bmatrix} \tilde{\mathbf{R}}_g^b \mathbf{R}_b^g & \tilde{\mathbf{R}}_g^b (\bar{\mathbf{V}}^g - \tilde{\mathbf{V}}^g) & \tilde{\mathbf{R}}_g^b (\mathbf{P}^g - \tilde{\mathbf{P}}^g) \\ \mathbf{0}_{1 \times 3} & 1 & 0 \\ \mathbf{0}_{1 \times 3} & 0 & 1 \end{bmatrix} = \begin{bmatrix} \tau_l^a & \tau_l^v & \tau_l^p \\ \mathbf{0}_{1 \times 3} & 1 & 0 \\ \mathbf{0}_{1 \times 3} & 0 & 1 \end{bmatrix} \in SE(3) \end{aligned} \quad (19)$$

where τ_l^a , τ_l^v , and τ_l^p denote the attitude, velocity, and position errors defined on left error model of Lie groups in the new LCEF frame.

Let ϕ_l denote the misalignment angle error of the left error model, with its skew-symmetric matrix as ψ_l ($\psi_l = [\phi_l \times]$). When ϕ_l is minimized, τ_l^a can be derived based on the relationship between Lie groups and Lie algebra:

$$\tau_l^a = \tilde{\mathbf{R}}_g^b \mathbf{R}_b^g = \exp(\phi_l \times) \approx \mathbf{I}_{3 \times 3} + \phi_l \times \quad (20)$$

$$\tau_l^v = \tilde{\mathbf{R}}_g^b (\bar{\mathbf{V}}^g - \tilde{\mathbf{V}}^g) = -\tilde{\mathbf{R}}_g^b \delta \bar{\mathbf{V}}^g \quad (21)$$

$$\tau_l^p = \tilde{\mathbf{R}}_g^b (\mathbf{P}^g - \tilde{\mathbf{P}}^g) = -\tilde{\mathbf{R}}_g^b \delta \mathbf{P}^g \quad (22)$$

where $\delta \bar{\mathbf{V}}^g = \tilde{\mathbf{V}}^g - \bar{\mathbf{V}}^g$ and $\delta \mathbf{P}^g = \tilde{\mathbf{P}}^g - \mathbf{P}^g$.

3.1.3. Analysis and selection of the Lie groups error model

The selection of the error model depends on the type of invariant observation, which are defined as follows:

$$\text{"leftinvariant" observation : } \mathbf{y} = \chi \cdot \mathbf{b} \quad (23)$$

$$\text{"rightinvariant" observation : } \mathbf{y} = \chi^{-1} \cdot \mathbf{b} \quad (24)$$

where \mathbf{b} is a constant vector.

If the observed vectors satisfy the "left-invariant" observation condition given in the first equation, the state left error model in the composite navigation combination is advantageous because the linearized observation model is independent of the global state χ . Conversely, if the observed vectors satisfy the "right-invariant" observation condition given in the second equation, the state right error model in the composite navigation model is more advantageous.

For the SINS/GNSS integrated navigation system, the GNSS system can provide velocity \mathbf{V}^g and position \mathbf{P}^g observation information in the LCEF frame. Considering that \mathbf{y} is constituted by velocity and position vectors, $\mathbf{y} = [\mathbf{V}^g \quad \mathbf{P}^g]^T$, the observation vector in the Lie groups can be represented as follows:

$$\begin{bmatrix} \mathbf{R}_b^g & \mathbf{V}^g & \mathbf{P}^g \\ \mathbf{0}_{1 \times 3} & 1 & 0 \\ \mathbf{0}_{1 \times 3} & 0 & 1 \end{bmatrix} \begin{bmatrix} \mathbf{0}_{3 \times 1} & \mathbf{0}_{3 \times 1} \\ 1 & 0 \\ 0 & 1 \end{bmatrix} = \begin{bmatrix} \mathbf{V}^g & \mathbf{P}^g \\ 1 & 0 \\ 0 & 1 \end{bmatrix} = \chi [\mathbf{b}_v \quad \mathbf{b}_p] \quad (25)$$

where χ is the state variables in (11) and \mathbf{b}_v , \mathbf{b}_p are constant vectors as follows:

$$[\mathbf{b}_v \quad \mathbf{b}_p] = \begin{bmatrix} \mathbf{0}_{3 \times 1} & \mathbf{0}_{3 \times 1} \\ 1 & 0 \\ 0 & 1 \end{bmatrix} \quad (26)$$

Both velocity and position observations satisfy the left-invariant observation definition.

The focus of integrated navigation is on attitude. Therefore, the definitions of left and right error models are discussed. The definitions of attitude error in the left and right error models are as follows:

$$\tau_l^a = \tilde{\mathbf{R}}_g^b \mathbf{R}_b^g \quad (27)$$

$$\tau_r^a = \mathbf{R}_b^g \tilde{\mathbf{R}}_g^b \quad (28)$$

According to the analysis using the matrix chain rule, the attitude error of the right error model, defined in the LCEF frame, can be expressed as $\mathbf{R}_b^g \tilde{\mathbf{R}}_g^b$. While the attitude error of the left error model, defined in the body frame (b-frame), can be expressed as $\mathbf{R}_g^b \tilde{\mathbf{R}}_g^g$. Attitude

error mainly originates from the gyroscope's measurement noise of the MEMS IMU, thus making the left error model more effective than the right error model.

Therefore, for the SINS/GNSS integrated navigation system in the LCEF frame, the left error model of the Lie groups SINS is more suitable.

3.2. Lie groups-based error equation

According to the analysis from the previous ijtf section, the LCEF frame Lie groups SINS left error model is more suitable for the INS/GNSS integrated navigation system. Therefore, using the LCEF frame Lie groups SINS left error model to derive the loosely coupled state equations, the attitude, velocity, and position errors in the LCEF frame Lie groups SINS left error model are obtained as follows:

$$\left. \begin{aligned} \tau_l^a &= \tilde{\mathbf{R}}_g^b \mathbf{R}_g^g \\ \tau_l^v &= -\tilde{\mathbf{R}}_g^b \delta \bar{\mathbf{V}}^g \\ \tau_l^p &= -\tilde{\mathbf{R}}_g^b \delta \mathbf{P}^g \end{aligned} \right\} \quad (29)$$

3.2.1. Lie groups-based attitude error equation

By differentiating both sides of equation (29) of the attitude error equation and combining it with the SINS attitude differential equation (10) in the LCEF frame, the attitude error equation can be derived as follows:

$$\dot{\phi}_l = -\tilde{\Omega}_{ab}^b \phi_l - \delta \omega_{ab}^b \quad (30)$$

where $\tilde{\Omega}_{ab}^b = \tilde{\omega}_{ab}^b \times$. Note $\tilde{\Omega}_{ab}^b$ as $\tilde{\Omega}^b$, $\tilde{\omega}_{ab}^b$ as $\tilde{\omega}^b$ in the following text.

3.2.2. Lie groups-based velocity error equation

By differentiating both sides of equation (29) of the velocity error equation, the following equation is obtained:

$$\dot{\tau}_l^v = -\tilde{\mathbf{R}}_g^b \delta \dot{\bar{\mathbf{V}}}^g - \tilde{\mathbf{R}}_g^b \delta \dot{\bar{\mathbf{V}}}^g \quad (31)$$

By differentiating the velocity differential equation from the SINS differential equation (10) in the LCEF frame, the following equation is obtained:

$$\delta \dot{\bar{\mathbf{V}}}^g = \delta \mathbf{R}_b^g \mathbf{f}^b + \mathbf{R}_b^g \delta \mathbf{f}^b - \Omega_{ag}^g \delta \bar{\mathbf{V}}^g \quad (32)$$

According to equation (20), writing matrix $\delta \mathbf{R}_b^g$ as follows:

$$\delta \mathbf{R}_b^g = -\tilde{\mathbf{R}}_b^g \phi_l \times \quad (33)$$

Substituting equation (33) into (32):

$$\delta \dot{\bar{\mathbf{V}}}^g = \tilde{\mathbf{R}}_b^g \mathbf{F}^b \phi_l - \tilde{\Omega}_{ag}^g \delta \bar{\mathbf{V}}^g + \tilde{\mathbf{R}}_b^g \delta \mathbf{f}^b \quad (34)$$

where $\mathbf{F}^b = \mathbf{f}^b \times$.

Substituting this into the original equation yields the velocity error equation:

$$\begin{aligned} \dot{\tau}_l^v &= -\tilde{\mathbf{R}}_g^b \delta \bar{\mathbf{V}}^g - \tilde{\mathbf{R}}_g^b \left(\tilde{\mathbf{R}}_b^g \mathbf{F}^b \phi_l - \tilde{\Omega}_{ag}^g \delta \bar{\mathbf{V}}^g + \tilde{\mathbf{R}}_b^g \delta \mathbf{f}^b \right) \\ &= \tilde{\Omega}_{gb}^b \tilde{\mathbf{R}}_g^b \delta \bar{\mathbf{V}}^g - \tilde{\mathbf{R}}_g^b \left(\tilde{\mathbf{R}}_b^g \mathbf{F}^b \phi_l - \Omega_{ag}^g \delta \bar{\mathbf{V}}^g + \tilde{\mathbf{R}}_b^g \delta \mathbf{f}^b \right) \\ &= -\mathbf{F}^b \phi_l - \tilde{\Omega}^b \tau_l^v - \delta \mathbf{f}^b \end{aligned} \quad (35)$$

3.2.3. Lie groups-based position error equation

By differentiating both sides of equation (29) of the position error equation, the following equation is obtained:

$$\dot{\tau}_l^p = -\tilde{\mathbf{R}}_g^b \delta \dot{\mathbf{P}}^g - \tilde{\mathbf{R}}_g^b \delta \dot{\mathbf{P}}^g \quad (36)$$

Differentiating the position differential equation from the SINS differential equation (10) in the LCEF frame, the following equation is obtained:

$$\delta \dot{\mathbf{P}}^g = \delta \bar{\mathbf{V}}^g - \Omega_{ag}^g \delta \mathbf{P}^g \quad (37)$$

Substituting the relevant equations into this, the position error equation is derived:

$$\begin{aligned} \dot{\tau}_l^p &= -\tilde{\mathbf{R}}_g^b \delta \dot{\mathbf{P}}^g - \tilde{\mathbf{R}}_g^b \left(\delta \bar{\mathbf{V}}^g - \Omega_{ag}^g \delta \mathbf{P}^g \right) \\ &= \tau_l^v - \tilde{\Omega}^b \tau_l^p \end{aligned} \quad (38)$$

The derived equations for attitude, velocity, and position errors are based on the Lie groups error model in the LCEF frame as following.

$$\begin{cases} \dot{\phi}_l = -\tilde{\Omega}^b \phi_l - \delta \omega^b \\ \dot{\tau}_l^v = -\mathbf{F}^b \phi_l - \tilde{\Omega}^b \tau_l^v - \delta \mathbf{f}^b \\ \dot{\tau}_l^p = \tau_l^v - \tilde{\Omega}^b \tau_l^p \end{cases} \quad (39)$$

4. Integrated navigation algorithm design and analyze

4.1. Lie groups-based integrated navigation algorithm

4.1.1. Lie groups-based state equation

According to equation (40), the Kalman filter state equation based on the Lie groups error model can be derived as follows:

$$\dot{\mathbf{X}}_l = \mathbf{F}_l \mathbf{X}_l + \mathbf{G}_l \mathbf{W}_l \quad (40)$$

where $\mathbf{X}_l = [\phi_l \quad \tau_l^v \quad \tau_l^p \quad \mathbf{e}^b \quad \nabla^b]^T$; \mathbf{F}_l , \mathbf{G}_l , and \mathbf{W}_l are the state matrix, noise matrix, and system noise, respectively, defined as follows:

$$\mathbf{F}_l = \begin{bmatrix} -\tilde{\Omega}^b & \mathbf{0}_{3 \times 3} & \mathbf{0}_{3 \times 3} & -\mathbf{I}_{3 \times 3} & \mathbf{0}_{3 \times 3} \\ -\tilde{\mathbf{F}}^b & -\tilde{\Omega}^b & \mathbf{0}_{3 \times 3} & \mathbf{0}_{3 \times 3} & -\mathbf{I}_{3 \times 3} \\ \mathbf{0}_{3 \times 3} & \mathbf{I}_{3 \times 3} & -\tilde{\Omega}^b & \mathbf{0}_{3 \times 3} & \mathbf{0}_{3 \times 3} \\ \mathbf{0}_{3 \times 3} & \mathbf{0}_{3 \times 3} & \mathbf{0}_{3 \times 3} & \mathbf{0}_{3 \times 3} & \mathbf{0}_{3 \times 3} \\ \mathbf{0}_{3 \times 3} & \mathbf{0}_{3 \times 3} & \mathbf{0}_{3 \times 3} & \mathbf{0}_{3 \times 3} & \mathbf{0}_{3 \times 3} \end{bmatrix} \quad (41)$$

$$\mathbf{G}_l = \begin{bmatrix} -\mathbf{I}_{3 \times 3} & \mathbf{0}_{3 \times 3} \\ \mathbf{0}_{3 \times 3} & -\mathbf{I}_{3 \times 3} \\ \mathbf{0}_{9 \times 3} & \mathbf{0}_{9 \times 3} \end{bmatrix} \quad (42)$$

$$\mathbf{W}_l = \begin{bmatrix} \mathbf{w}_g \\ \mathbf{w}_a \end{bmatrix} \quad (43)$$

where \mathbf{w}_g denotes white noise in angular velocity measurement using the gyroscope, and \mathbf{w}_a denotes white noise in specific force measurement using the accelerometer.

4.1.2. Lie groups-based measurement equation

The difference in auxiliary velocity and position calculated by the inertial navigation system and satellite navigation system is selected as the measurement vector. The Lie groups-based measurement equation for SINS/GNSS is as follows:

$$\mathbf{Z}_l = \mathbf{H}_l \mathbf{X}_l + \mathbf{V}_l \quad (44)$$

where \mathbf{Z}_l represents the measurement vector, and \mathbf{V}_l represents the measurement noise of GNSS.

The measurement vector \mathbf{Z}_l can be obtained by subtracting the auxiliary velocity vector $\hat{\mathbf{V}}^g$ of SINS from the GNSS auxiliary velocity vector $\bar{\mathbf{V}}^g$ of GNSS as well as subtracting the position vector $\hat{\mathbf{P}}^g$ of SINS from the position information of GNSS \mathbf{P}^g provided by the satellite navigation system.

$$\mathbf{Z}_l = \begin{bmatrix} \hat{\mathbf{V}}^g - \bar{\mathbf{V}}^g \\ \hat{\mathbf{P}}^g - \mathbf{P}^g \end{bmatrix} = \begin{bmatrix} \delta \bar{\mathbf{V}}^g \\ \delta \bar{\mathbf{P}}^g \end{bmatrix} \quad (45)$$

The measurement noise vector \mathbf{V}_l includes the white noise of auxiliary velocity $\bar{\mathbf{v}}_v$ and position \mathbf{v}_p from the GNSS. $\mathbf{V} = [\bar{\mathbf{v}}_v, \mathbf{v}_p]^T$.

$$\bar{\mathbf{v}}_v = \mathbf{v}_v + \boldsymbol{\Omega}_{ag}^g \mathbf{v}_p \quad (46)$$

where \mathbf{v}_v represents the white noise in velocity measurement from the GNSS. From the definition of the left error in Equation (29), matrix \mathbf{H}_l can be obtained:

$$\mathbf{H}_l = \begin{bmatrix} \mathbf{0}_{3 \times 3} & -\hat{\mathbf{R}}_b^g & \mathbf{0}_{3 \times 3} & \mathbf{0}_{3 \times 3} & \mathbf{0}_{3 \times 3} \\ \mathbf{0}_{3 \times 3} & \mathbf{0}_{3 \times 3} & -\hat{\mathbf{R}}_b^g & \mathbf{0}_{3 \times 3} & \mathbf{0}_{3 \times 3} \end{bmatrix} \quad (47)$$

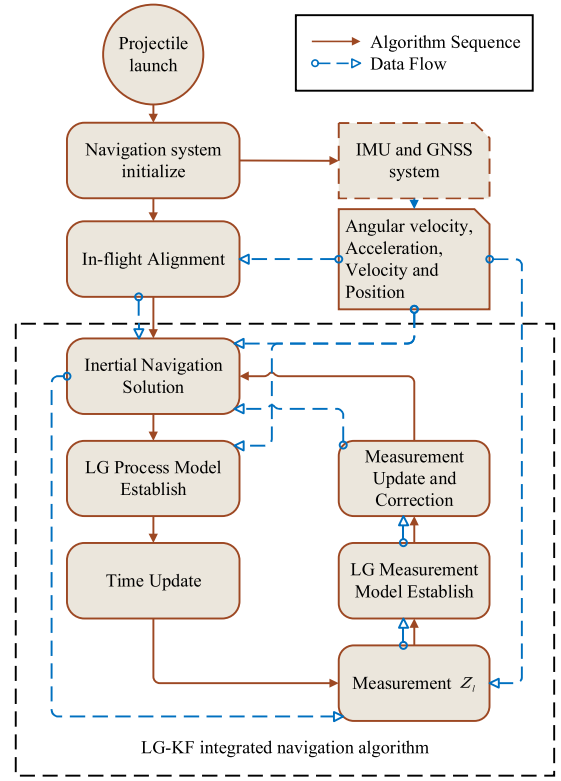


Fig. 2. Flowchart of the LG-KF Algorithm.

4.2. Error propagation analysis

In the following discussion, the error propagation of LG-KF and EKF are compared, demonstrating the advantage of left error model in SINS/GNSS integrated navigation.

The most common method in integrated navigation is EKF established in small-perturbation approximation, which may not converge under large misalignment. The failure of traditional navigation algorithm is primarily caused by the invalidation of navigation model. Invalidation is attributable to two key factors. First, the traditional navigation linear model is established in small-perturbation

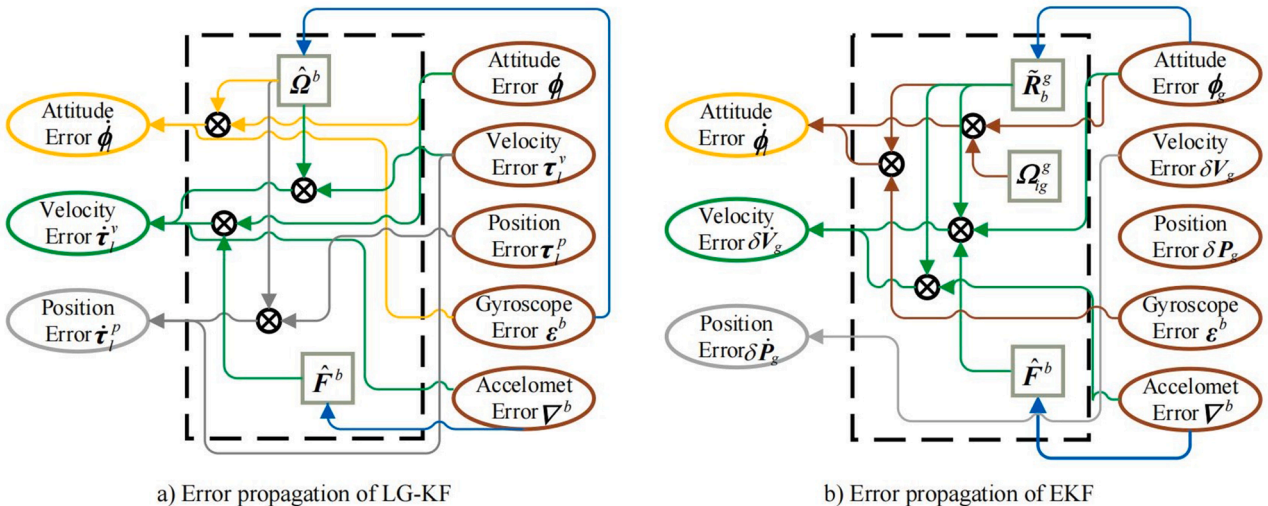


Fig. 1. Error propagation comparison.

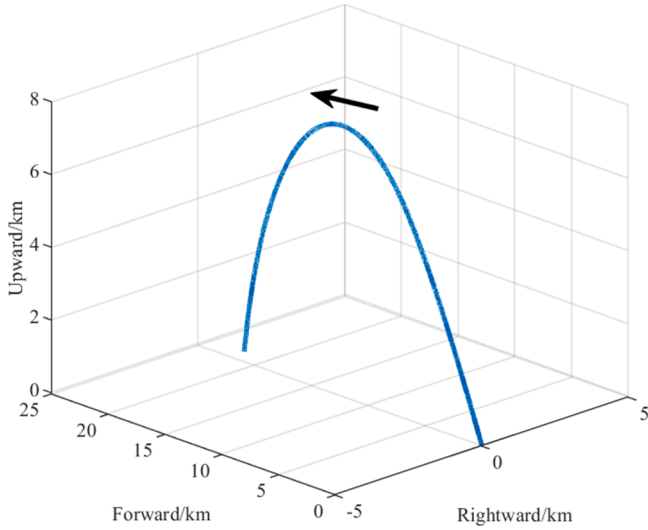


Fig. 3. Simulation trajectory of the guided projectile.

approximation, and the character of nonlinear navigation model is not accurately described in the linear models. Second, the parameter used in linear models is obtained using SINS through approximation. Large misalignment indicates that large error will be introduced into the navigation system if the attitude matrix is used as a part of the navigation model parameter.

The error propagation of EKF[19] and LG-KF based on the state equation are shown in Fig. 1.

The state matrix of the EKF incorporates Ω_{eg}^g (skew-symmetric matrix of earth rotation angular velocity ω_{eg}^g), R_b^g (attitude matrix), and F^b (skew-symmetric matrix of specific force f^b) as inherent parameters. Exponentially, \tilde{R}_b^g provided by SINS is not an efficient approximation of R_b^g under large misalignment. Hence, traditional EKF fails to estimate the misalignment angles ϕ^g . The LG-KF employing SE(3) formulations exhibits distinct state-space characteristics. Its mechanization directly integrates \tilde{F}^b (accelerometer outputs) and $\hat{\Omega}_{ib}^b$ (gyroscope outputs) as inherent parameter, decoupling state equation parameters from initial misalignment. This differential geometric architecture demonstrates enhanced robustness against nonlinear approximation errors induced by large misalignment. Consequently, ability of misalignment estimation is enhanced.

4.3. Algorithm design

This section presents the algorithm design of the LG-KF, transforming theoretical models to software components for HVPs. Aligned with the GNC cycle of HVPs' navigation systems, Figure 2 delineates the workflow of the navigation system:

The algorithm design is shown in Fig. 2. The thermal battery of HVP is activated after launch, before the navigation system initialized. When both IMU data and GNSS data are valid, in-flight alignment begins. Upon convergence of the in-flight alignment process, the initialized navigation states – including alignment attitude, GNSS velocity and position– are propagated into the SINS and to start SINS/GNSS integrated navigation.

Then the LG-KF integrated navigation algorithm run as follow:

Table 2
Parameters for SINS/GNSS.

Parameter	Value	Parameter	Value
Gyroscope bias	200°/h	Accelerometer Bias	10 mg
Angular random walk	20°/√h	Accelerometer random noise	6 mg
Gyroscope scale factor error	120ppm	Accelerometer scale factor error	240 ppm
Gyroscope mounting error	6'	Accelerometer mounting error	6'
GNSS position error	8m	GNSS velocity error	0.3 m/s

1ppm=10⁻⁶.

Table 3
Initial error settings.

Parameter	Number	Parameter	Number
Roll error	30°	Position error	40 m
Pitch error	10°	Velocity error	1.5 m/s
Yaw error	10°		

1. Establish LG process model and obtain state matrix as equation (41).
2. Time update. Equations are given as follows, which are the same as standard KF.

$$\begin{cases} \hat{\mathbf{X}}_{k/k-1} = \Phi_{k/k-1} \hat{\mathbf{X}}_{k-1} \\ \mathbf{P}_{k/k-1} = \Phi_{k/k-1} \mathbf{P}_{k-1} \Phi_{k/k-1}^T + \mathbf{Q}_{k-1} \end{cases} \quad (48)$$

Where $\Phi_{k/k-1} \approx \mathbf{I} + \mathbf{F}_l(t_k)$.

3. Measurement $\mathbf{Z}_k = \mathbf{Z}_l(t_k)$ computation as equation(45) upon GNSS epoch detected.
4. Measurement equation computation as equation(47).
5. Measurement update and correction. Equations are given as follows.

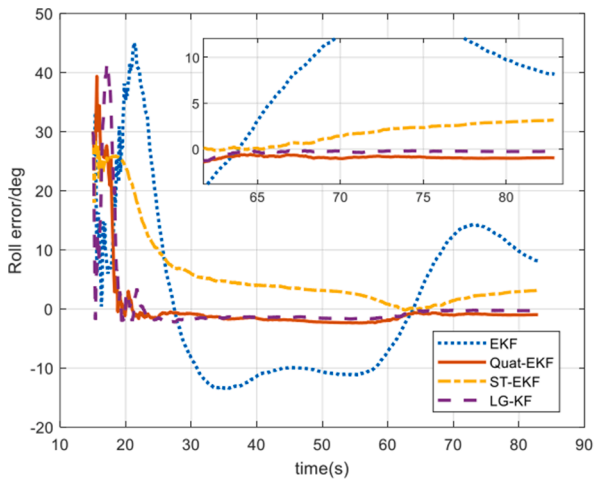
$$\begin{cases} \mathbf{K}_k = \mathbf{P}_{k/k-1} \mathbf{H}_k^T (\mathbf{H}_k \mathbf{P}_{k/k-1} \mathbf{H}_k^T + \mathbf{R}_k)^{-1} \\ \hat{\mathbf{X}}_k = \hat{\mathbf{X}}_{k/k-1} + \mathbf{K}_k (\mathbf{Z}_k - \mathbf{H}_k \hat{\mathbf{X}}_{k/k-1}) \\ \mathbf{P}_k = (\mathbf{I} - \mathbf{K}_k \mathbf{H}_k) \mathbf{P}_{k/k-1} \end{cases} \quad (49)$$

As the time update and measurement update are the same as standard KF, the computational cost is on the same magnitude as EKF.

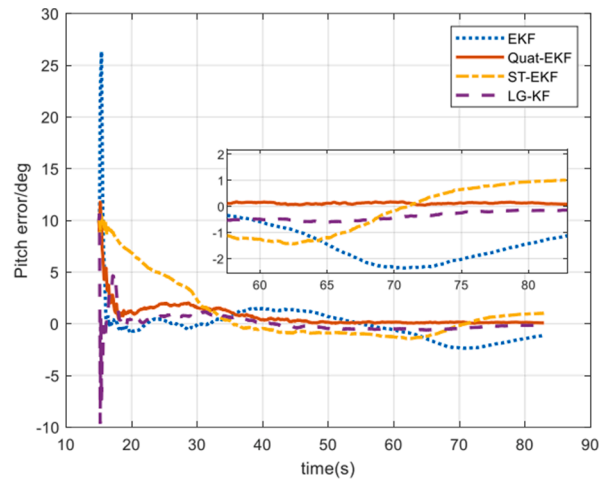
Explicit pseudocode is attached in Appendix 1.

5. SINS/GNSS Integrated Navigation Experiment

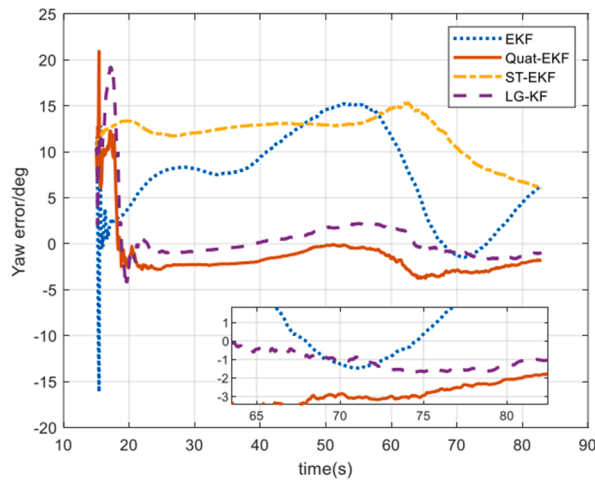
To validate the algorithm design proposed in this paper, comprehensive verification was conducted through numerical simulations and vehicle road tests. The simulation outcomes are shown in section 5.1, and the road test experiment results are analyzed in Section 5.2.



a) Roll error of the four algorithms

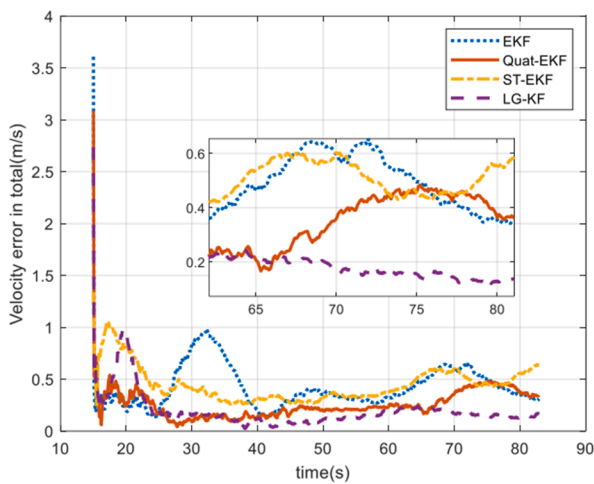


b) Pitch error of the four algorithms

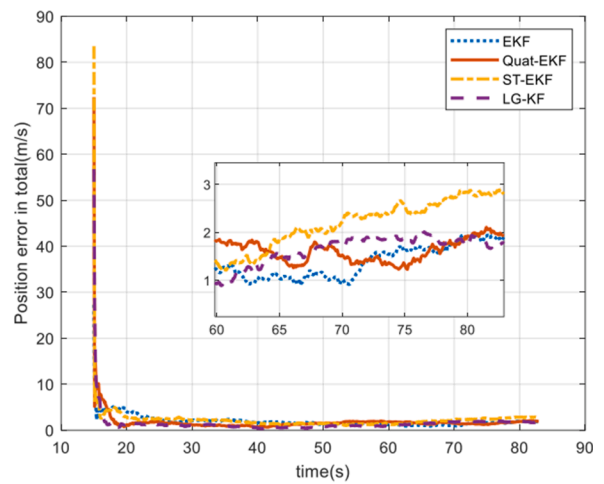


c) Yaw error of the four algorithms

Fig. 4. Simulation results for [30, 10, 10] degrees misalignment angles.



a) Total velocity error of the four algorithms



b) Total position error of the four algorithms

Fig. 5. Total velocity and position errors for [30,10,10] degrees misalignment angles.

Table 4
Initial error settings.

Parameter	Number	Parameter	Number
Roll error	140°	Position error	40 m
Pitch error	15°	Velocity error	1.5 m/s
Yaw error	15°		

5.1. Experimental trajectory and parameters

Four methods are compared: the traditional Extended Kalman Filter (EKF), State Transformation Extended Kalman Filter (ST-EKF), quaternion-based integrated navigation algorithm (Quat-EKF), and Lie groups-based integrated navigation algorithm (LG-KF). The trajectory is shown in Fig. 3.

IMU and satellite navigation parameter setting are shown in Table 2.

5.1.1. Experiment in misalignment of [30°, 10°, 10°]

The first experiment examines the precision of the four algorithms. The initial error settings are shown in Table 3.

The results are illustrated in Fig. 4.

As shown in Fig. 4, under the given misalignment angles of [30, 10, 10] degrees, all four algorithms maintain their navigation functionality. Regarding attitude errors, all algorithms demonstrate convergence, with

yaw angle convergence precision being lower than that of pitch and roll. Specifically, Quat-EKF and LG-KF show similar yaw angle errors, ranging from 1° to 2°, while EKF and ST-EKF exhibit larger errors, around 6°. The final pitch and roll errors for LG-KF are -0.102° and -0.407°, respectively, while for Quat-EKF, they are 0.114° and -0.331°, respectively. In terms of convergence accuracy for yaw and roll, Quat-EKF and LG-KF are similar and significantly outperform EKF and ST-EKF. The velocity and position errors of the four algorithms are shown as Fig. 5.

As the GNSS provide velocity and position measurements, the total errors in velocity and position for all four methods converge.

5.1.2. Experiment in misalignment of [140°, 15°, 15°]

The second experiment examines the convergence of the four algorithms under large misalignment conditions. The initial error settings are shown in Table 4.

The results are illustrated in Fig. 6.

Simulation results indicate that traditional EKF fails to converge in attitude under large misalignment angles of [140, 15, 15] degrees, completely losing its attitude navigation functionality. Quat-EKF fails to converge on yaw angle, while pitch and roll errors reduce slightly but fail to converge stably, exhibiting fluctuations of ±50° between 50 and 83 seconds. In comparison, the ST-EKF algorithm achieves convergence of pitch and roll errors to 0.193° and -1.282°, respectively, and yaw to

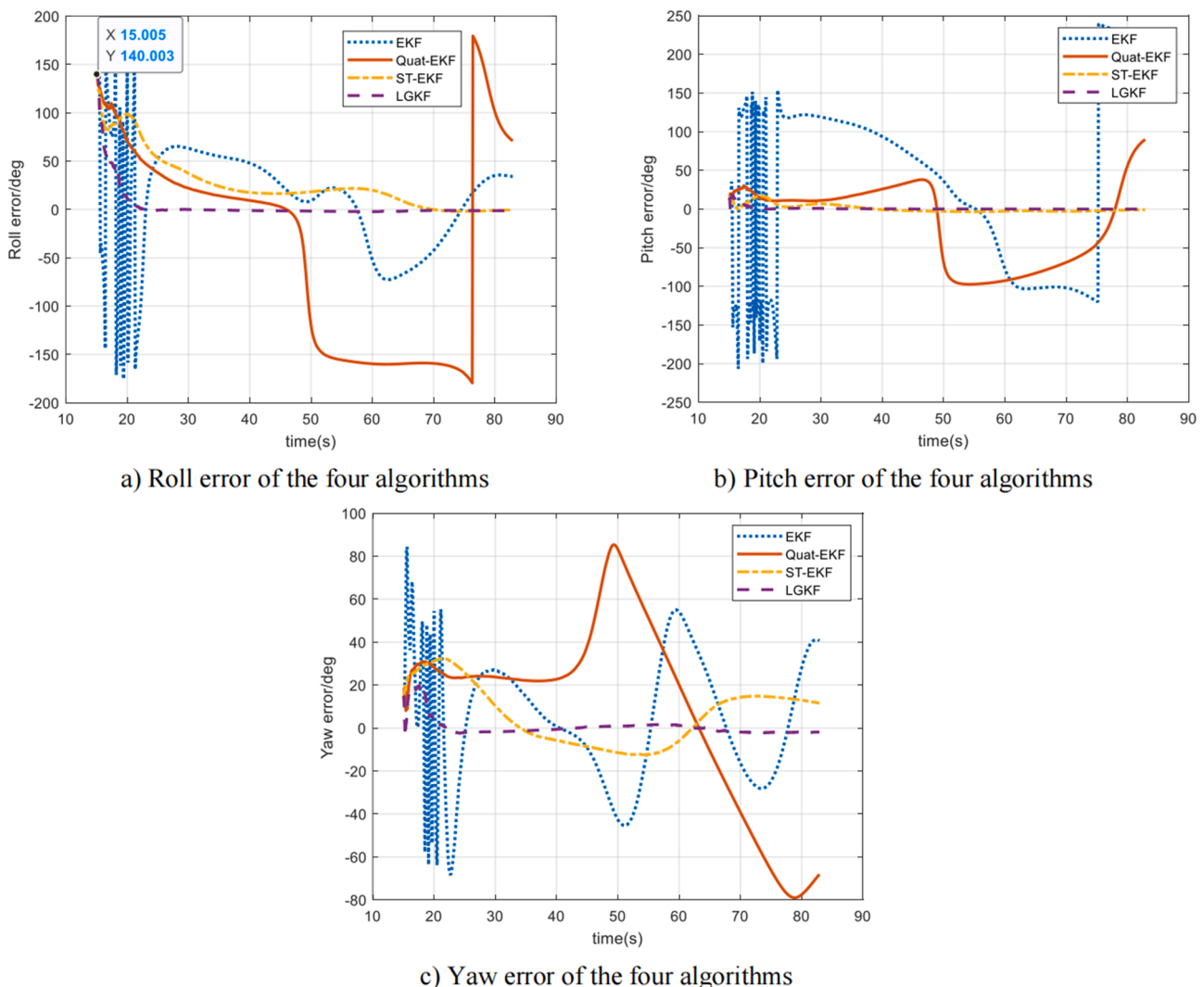
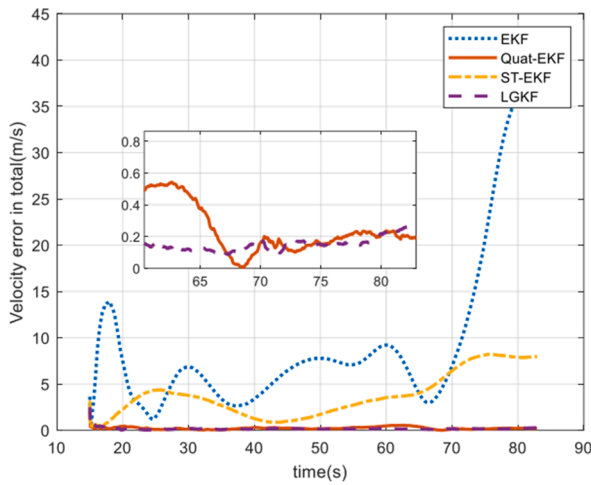
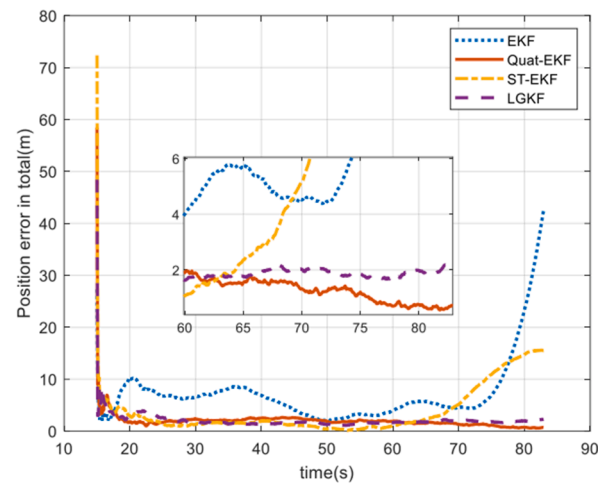


Fig. 6. Simulation results for [140,15,15] degrees misalignment angles.



a) Total velocity error of the four algorithms



b) Total position error of the four algorithms

Fig. 7. Total velocity and position errors for [140,15,15] degrees misalignment angles.

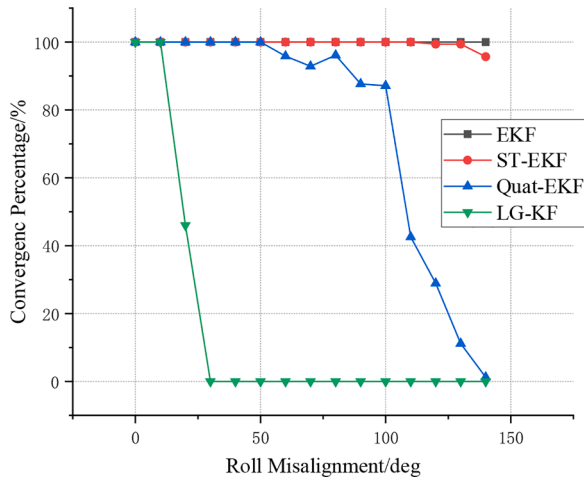


Fig. 8. Convergency percentage changes with roll misalignment.

11.651°. The LG-KF algorithm achieves convergence of pitch and roll errors to -0.141° and 0.213° , and yaw to -0.257° . Quat-EKF and LG-KF demonstrate navigation capabilities under large misalignment angles similar to [30, 10, 10] accuracy levels. The velocity and position errors of the four algorithms are shown as Fig. 7.

EKF and ST-EKF still exhibit large errors in velocity and position even when velocity and position data are provided by GNSS. This can be attributed to the divergence of inertial navigation attitude errors, which renders the inertial navigation information unreliable. Additionally, large linearization inaccuracies invalidate the filtering model, contributing to the divergence of EKF and ST-EKF, as linearization errors are not considered in the inertial navigation error equations. By contrast, Quat-EKF and LG-KF demonstrate stable convergence of velocity and position errors.

Table 5

Convergence range, precision, and time for four algorithms.

Algorithms	Errors	Initial error range for convergence/ $^\circ$	RMS for convergence (1σ) / $^\circ$	Time for convergence /s
EKF	Pitch error	$\pm 6^\circ$	0.531 $^\circ$	10
	Yaw error	$\pm 6^\circ$	3.679 $^\circ$	10
	Roll error	$\pm 10^\circ$	1.314 $^\circ$	20
Quat-EKF	Pitch error	$\pm 15^\circ$	0.794 $^\circ$	20
	Yaw error	$\pm 15^\circ$	1.940 $^\circ$	10
	Roll error	$\pm 50^\circ$	0.567 $^\circ$	10
ST-EKF	Pitch error	$\pm 15^\circ$	0.592 $^\circ$	15
	Yaw error	$\pm 15^\circ$	6.061 $^\circ$	15
	Roll error	$\pm 110^\circ$	2.516 $^\circ$	20
LG-EKF	Pitch error	$\pm 15^\circ$	0.073 $^\circ$	10
	Yaw error	$\pm 15^\circ$	0.878 $^\circ$	10
	Roll error	$\pm 140^\circ$	0.475 $^\circ$	10

5.1.3. Misalignment bias experiment comparison of four algorithms

The third experiment investigates the convergence range of the four algorithms. The algorithm uses 3,509 ($29 \times 11 \times 11$) sets of misalignment bias parameters to simulate the convergence behavior of LG-KF, EKF, Quat-EKF and ST-EKF. The yaw angle is set within the range of -140 to 140 degrees, with points sampled every 10 degrees (29 points). The pitch angle ranges from -15 to 15 degrees, with points sampled at intervals of 3 degrees (11 points). The convergence percentage changed



Fig. 9. Road test trajectory shown on the map.



Fig. 10. Equipment used in the road test.

with the roll misalignment of the four algorithms are shown in Fig. 12. For more detail of the bias experiment, please refer to appendix 4.

As is shown in Fig. 8, results of EKF converge with yaw and pitch misalignment errors no more than 6° , and roll misalignment error no more than 10° . When the roll misalignment exceeds 10° , the convergence percentage of EKF decreased. ST-EKF and Quat-EKF performs better than EKF, and the LG-KF perform the best. All the results of Quat-EKF converge when the roll error 50° , ST-EKF suit the misalignment of 110° , while proposed in this paper LG-KF works when the roll misalignment is 140° .

The initial error range, precision and time for convergence of the four algorithms are summarized in Table 5.

The simulation results and Table 5 indicate that the LG-KF algorithm in the LCEF frame achieves effective convergence with the largest roll misalignment of 140° . By contrast, the other three algorithms exhibit varying degrees of accuracy degradation when roll angle errors exceed 110° . The EKF, Quat-EKF, and ST-EKF algorithms exhibit a large number of divergent results. Meanwhile, the Lie groups algorithm achieves convergence of navigation attitude errors under large misalignment angles without significant degradation in convergence accuracy.

5.2. Car-mounted road test.

The road test was conducted in Xi'An on a vehicle platform using an INS/GNSS system. The INS system used MEMS gyroscope and accelerometer and the GNSS receiver was UR4B0 of BDStar navigation. The sampling frequency of the INS was set to 400 Hz, and the sampling frequency of the GNSS was 10 Hz. A main INS with ring laser gyroscope and quartz flexible accelerometer provided high-precision navigation information as a reference. The specific parameters are shown in Table 6 in appendix 3. A typical road experiment for 500s was carried out. First, the main INS performs initial alignment for 300 s when the car was parking. Then, the main INS shifts to the INS/GNSS integrated navigation mode, and the car began to move forward on the road. When the car was moving, the power of MEMS INS was connected, and its output was received on the computer for 105s. After the road test, the IMU data and the GNSS data were loaded in real-time simulation software Links-RT and sent to the navigation embedded computer at 400 Hz through an industrial control computer Links-C3U. The four algorithms discussed in section 4.1 were loaded on the navigation embedded computer, and the results were shown in Figs. 11 and 12. The initial attitude of MEMS SINS was set as $[140^\circ, 15^\circ, 15^\circ]$, while the attitude provided by the main INS was $[0.206^\circ, -0.393^\circ, -5.292^\circ]$.

The road test trajectory in Kunming Road of Xi'An is shown in Fig. 9.

The facilities of road test are displayed in Fig. 10:

The results are illustrated in Fig. 11 and Fig. 12.

The attitude error obtained in the test are shown in Figs. 11 and 12. Overall, the road test yielded better results than simulations, with LG-KF demonstrating the best performance. The attitude error in LG-KF can rapidly converge to near 0° , which is notably better than the other three algorithms. Moreover, the other three algorithms exhibit considerably lower convergence speeds, and the yaw error of EKF and Quat-EKF are not converge until the end of the test because the approximation in state model is not suitable for large misalignment angles.

The RMS of the attitude error from 50 s to 105 s is shown in Table 7. LG-KF demonstrates notable advantages over EKF, Quat-EKF and LG-KF. When the misalignment angle variance is $[140^\circ, 15^\circ, 15^\circ]$, the yaw accuracy is improved by 94.1%, 95.5%, and 88.1%, respectively. The roll accuracy is improved by 85.1%, 83.6 %, and 3.9 %, respectively, and the pitch accuracy is improved by 35.6%, 84.2 %, and 82.0 %, respectively.

6. Conclusion

This paper presents a Lie groups-based SINS/GNSS algorithm in the

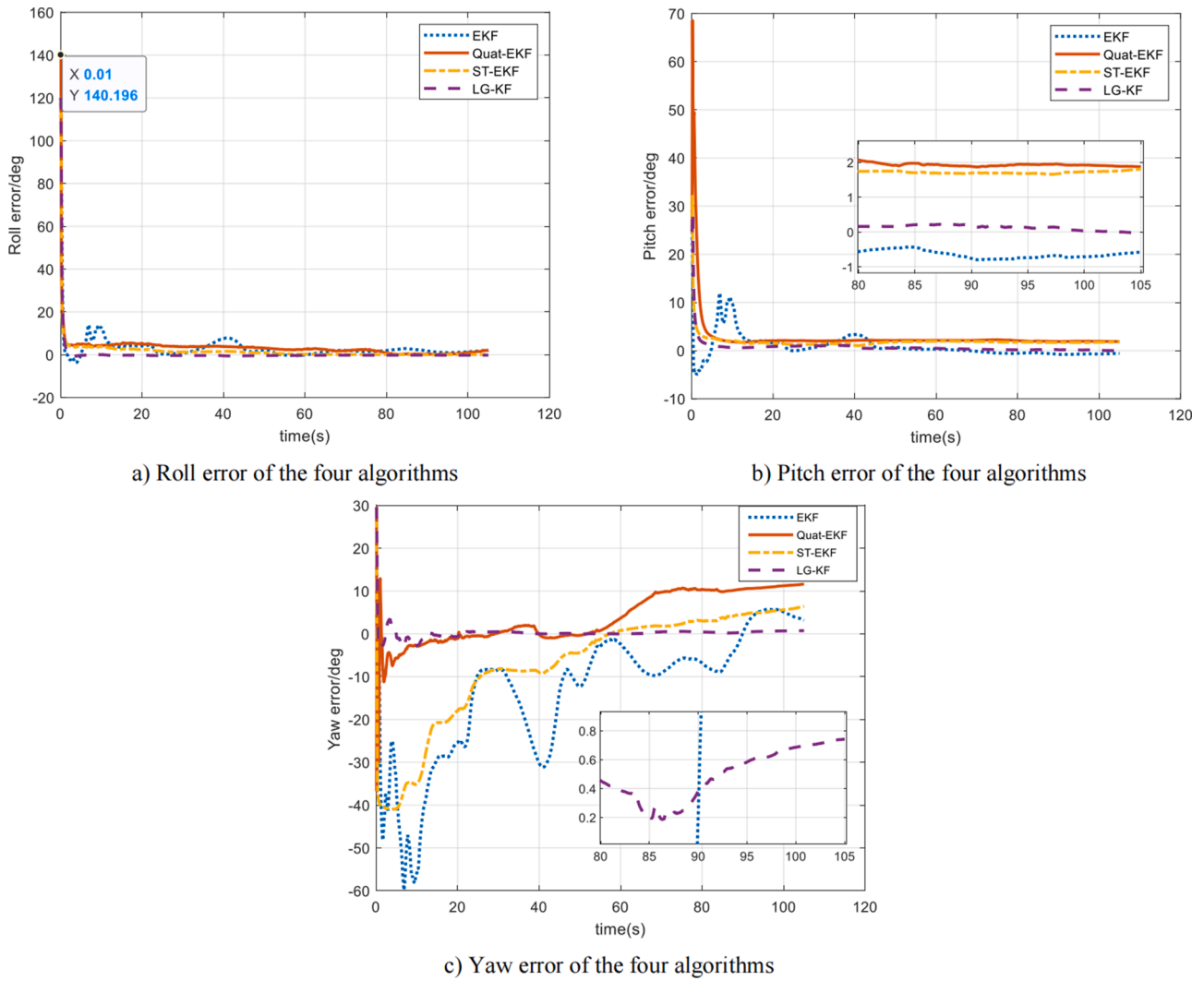


Fig. 11. Road test results for [140,15,15] degrees misalignment angles.

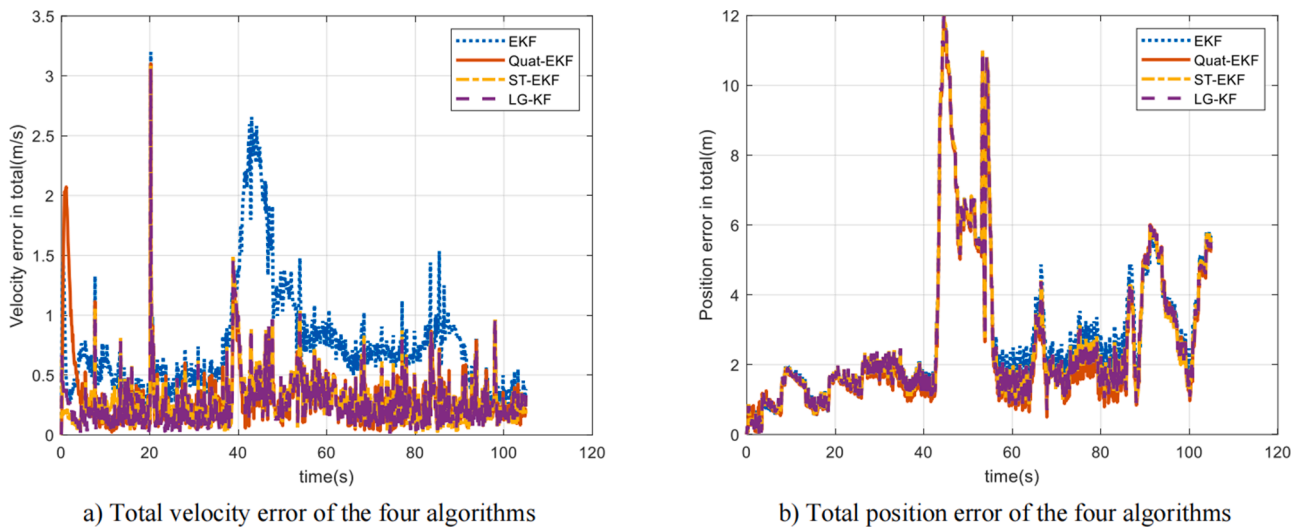


Fig. 12. Total velocity and position errors in the road test.

LCEF frame for integrated navigation of guided projectiles under conditions of large misalignment. Simulation experiments and a road test are conducted to compare traditional methods such as EKF, Quat-EKF,

and ST-EKF with the LG-KF algorithm. LG-FK in the LCEF frame proposed in this paper outperforms among the four algorithms in large misalignment scenery.

Table 7

Attitude RMS in the road test in 50-105 s.

	Roll error/ $^{\circ}$	Yaw error/ $^{\circ}$	Pitch error/ $^{\circ}$
EKF	1.640	6.490	0.503
Quat-EKF	1.495	8.741	2.058
ST-EKF	0.235	3.243	1.805
LG-KF	0.245	0.389	0.324

LG-KF in the LCEF frame presents high-precision convergence and strong robustness under large roll misalignment. The simulation and the road test both demonstrate that the Lie groups algorithm consistently converges with high accuracy when roll misalignment amount to 140° , exhibiting notable navigational advantages among the four algorithms. This will help HVPs maintain stable integrated navigation when in-flight alignment accuracy degrades, addressing the challenges posed by poor IMU performance and extreme launch conditions.

Although simulation and the road test results confirm that the LG-KF algorithm in the LCEF frame effectively addresses integrated navigation challenges for guided projectiles under large misalignment angles, navigation result sometimes fails to converge in extreme misalignment (such as roll misalignment 180°). Besides, the LG-KF algorithm may exhibit reduced robustness under extreme gyroscopic performance degradation scenarios, particularly when gyroscope bias instability exceeds $2000^{\circ}/\text{h}$ or angle random walk surpasses $100^{\circ}/\sqrt{\text{h}}$. In the future work, the algorithm should be improved to ensure the convergence in

Appendix

Appendix 1

In this appendix, we provide the pseudocode for the algorithm proposed in this paper as [Algorithm 1](#).

Algorithm 1

LG-KF integrated navigation processing flow.

```

Input: IMU Data Flow, GNSS Data Flow
Output: Attitude(Att), Velocity(Vel), Position(Pos)
Procedure Main()
  InitPara()           //System initialize
  while SystemOperate do // Main Loop
    if T_flag == 1 then //Timer-triggered Interrupt
      imu ← GetImuData(IMU) // Get IMU data
      gnss ← GetGnssData(GNSS) // Get GNSS data
      if SystemTime < 10 then // In flight Alignment stage
        InflightAlignment(gnss, imu)
      else // integrated navigation stage
        Att, Vel, Pos ← SINS(imu)
        phi_LG ← CalculateLeverArm(imu, Att, Vel, Pos)
        Xk ← StateUpdate(Xk, phi_LG)
        Xk ← MeasurementUpdate(Xk, Zk)
        Att, Vel, Pos ← AVPCompensate(Att, Vel, Pos, Xk)
      end if
    end if
  end while
end Procedure

```

Appendix 2

In this appendix, we provide a detailed description of the trajectory, initial conditions, and sensor noise characteristics (e.g., bias, scale factor, noise level), along with their modeling approaches in the simulation.

In this simulation, we designed a near-parabolic trajectory lasting 83 seconds, with a launch latitude of 34.2° , longitude of 108.9° , altitude of 400 meters, and an azimuth of 0° . The highest point of the trajectory reaches an altitude of 7.8 km, and the distance from the launch point to the impact point is 22.199 km. The trajectory is shown in [Fig. 3](#), with the launch point at the origin. Simulation data from 16 to 83 seconds is used for integrated navigation.

extreme misalignment. It is also worth noting that the algorithm's performance—encompassing convergence time, convergence accuracy, and robustness against large misalignment angles—may vary depending on motion trajectories and IMU specifications, requiring case-specific analysis in practical applications.

CRedit authorship contribution statement

Kai Chen: Validation, Resources, Project administration, Methodology, Funding acquisition, Formal analysis, Data curation. **Chengzhi Zeng:** Writing – original draft, Software, Methodology, Data curation. **Peng Huang:** Data curation, Conceptualization. **Zhenhao Li:** Software, Investigation, Data curation. **Jiang He:** Methodology, Investigation, Data curation.

Declaration of competing interest

The authors declare the following financial interests/personal relationships which may be considered as potential competing interests:

Kai Chen reports financial support was provided by National Natural Science Foundation of China. If there are other authors, they declare that they have no known competing financial interests or personal relationships that could have appeared to influence the work reported in this paper.

The velocity and attitude curves are as Fig. 13:

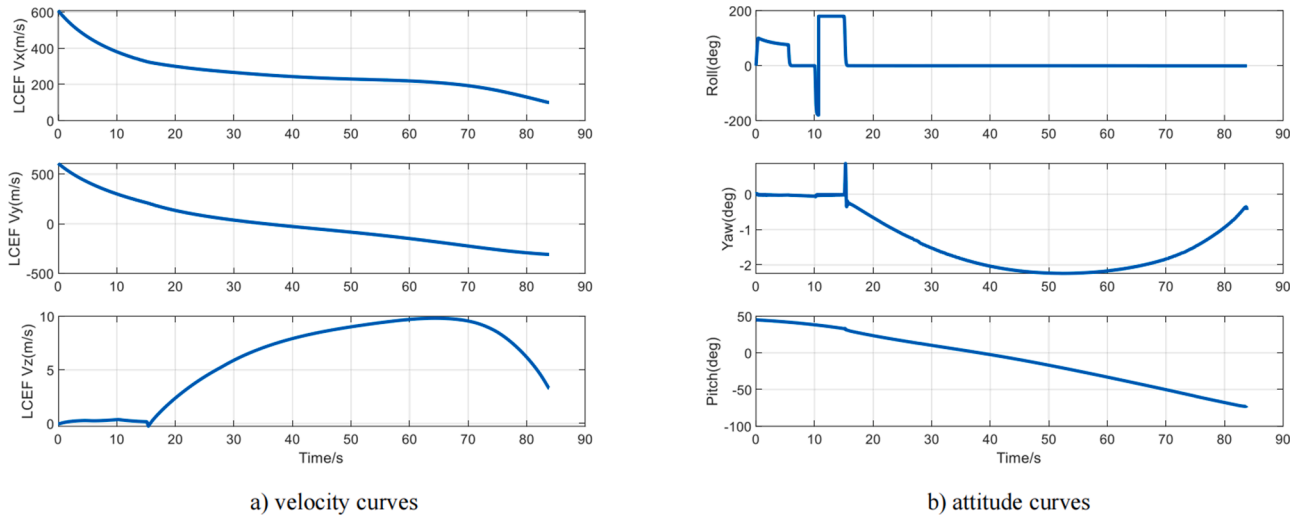


Fig. 13. velocity and attitude curves of trajectory.

The error model of IMU in Table 2 is shown as below:

1. *error model of gyroscope.* Gyroscope are angular rate sensor, and the relationship between true angular rate ω_{ib}^b and measured values of gyroscope $\tilde{\omega}_{ib}^b$ can be described as follows:

$$\tilde{\omega}_{ib}^b = \omega_{ib}^b + \delta\omega_{ib}^b \quad (50)$$

Where $\delta\omega_{ib}^b$ is given as follows:

$$\delta\omega_{ib}^b = \mathbf{b}_g + \mathbf{S}_g\omega_{ib}^b + \mathbf{N}_g\omega_{ib}^b + \boldsymbol{\varepsilon}_g \quad (51)$$

Where \mathbf{b}_g is gyroscope bias; \mathbf{S}_g is scale factor error matrix; \mathbf{N}_g is the mounting error matrix of the gyroscope; $\boldsymbol{\varepsilon}_g$ is gyroscope noise. \mathbf{S}_g and \mathbf{N}_g are given as follow:

$$\mathbf{N}_g = \begin{bmatrix} 0 & \theta_{g,xy} & \theta_{g,yz} \\ \theta_{g,yx} & 0 & \theta_{g,yz} \\ \theta_{g,zx} & \theta_{g,zy} & 0 \end{bmatrix} \quad (52)$$

$$\mathbf{S}_g = \begin{bmatrix} s_{g,x} & 0 & 0 \\ 0 & s_{g,y} & 0 \\ 0 & 0 & s_{g,z} \end{bmatrix} \quad (53)$$

Where $\theta_{g,(i)}$ is non-orthogonal of two gyroscopes, $s_{g,(i)}$ is the scale factor of a single gyroscopes.

2. *error model of accelerometer*

Gyroscope are angular rate sensor, and the relationship between true specific force \mathbf{f}^b and measured values of accelerometer $\tilde{\mathbf{f}}^b$ can be described as follows:

$$\tilde{\mathbf{f}}^b = \mathbf{f}^b + \delta\mathbf{f}^b \quad (54)$$

Where $\delta\mathbf{f}^b$ is given as follows:

$$\delta\mathbf{f}^b = \mathbf{b}_a + \mathbf{S}_1\mathbf{f}^b + \mathbf{S}_2\mathbf{f}_2 + \mathbf{N}_a\mathbf{f}^b + \delta\mathbf{g} + \boldsymbol{\varepsilon}_a \quad (55)$$

Where \mathbf{b}_a is accelerometer bias; \mathbf{S}_a is scale factor error matrix; \mathbf{N}_a is the mounting error matrix of the accelerometer; $\boldsymbol{\varepsilon}_a$ is accelerometer noise. \mathbf{S}_a and \mathbf{N}_a are similar to \mathbf{S}_g and \mathbf{N}_g .

Appendix 3

In this appendix, we provide a detailed description road test, including sensor specifications, test trajectory, and data collection method.

1. *Sensor specifications of road test.* The sensor specifications of Main SINS and MEMS IMU are shown in Tabel 6.

Table 6
sensors precision of the Main SINS.

Parameter	Main INS	MEMS IMU
Gyroscope Bias	0.005"/h	200"/h
Gyroscope random walk	0.0008"/ \sqrt{h}	20"/ \sqrt{h}
Gyroscope scale factor error	20ppm	120ppm
Gyroscope mounting error	10"	6'
Accelerometer bias	30ug	10 mg
Accelerometer noise	10ug	6 mg
Accelerometer scale factor error	10ppm	240 ppm
Accelerometer mounting error	10"	6'

2. Work state of Main SINS and MEMS IMU. As is shown in Fig 10 The main SINS is mounted on the vehicle via an adapter plate, with a forward reference surface ensuring consistent alignment of the INS in both forward and upward orientations.

The reference ring laser gyroscope-based inertial navigation system (RLG-INS) and the MEMS-INS under test were both connected to GNSS signals, synchronized to satellite time. The INS and GNSS utilized a pulse synchronization method, where the GNSS receiver transmits a pulse synchronization signal to the INS via a TTL interface upon acquiring satellite signals. During integrated navigation, the INS data sampled at the rising edge of the PPS (Pulse Per Second) signal was combined with GNSS measurements to construct observation vectors for the LG-KF (Loose-GPS/Kalman Filter), enabling real-time fusion navigation.

3. Data collection and test method. The complete vehicle test data spans 15 minutes, with the starting point coordinates at (latitude: 34.24530029 degree, longitude: 108.8961945 degree) and the endpoint at (latitude: 34.24209976 degree, longitude: 108.9019547 degree). For algorithm validation, a straight-line segment from the middle of the test data was selected, meaning the MEMS-INS began navigation when the vehicle was already in motion. The initial velocity and position values of the MEMS-INS were provided by satellite navigation, while the initial attitude values were derived from the reference INS attitude with intentionally introduced errors: 15° in pitch/yaw and 140° in roll.

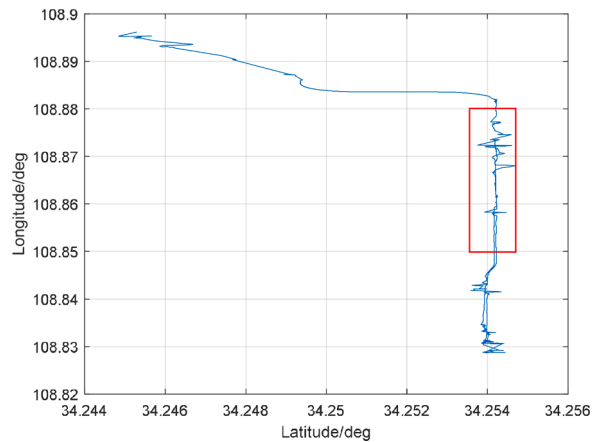


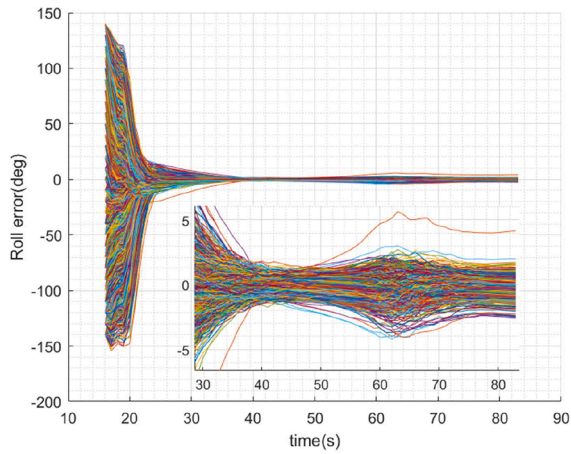
Fig. 14. Road test trajectory for 15 minutes.

The segment enclosed by the red box is the one used in the experiment, which is shown in Fig. 14.

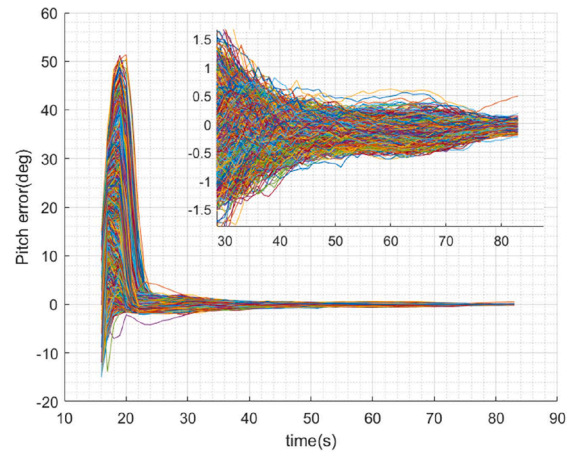
Appendix 4

The 3509 times of bias experiment attitude error results curve of all four algorithm and the experimental is shown below.

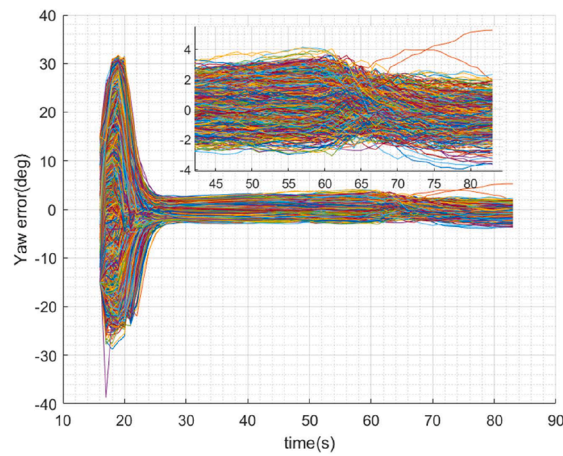
The diverging results are indicated by the gray line and the converge result are indicated by various color in the graph. The results of the LG-KF algorithm are illustrated in Fig. 15.



a) Roll error



b) Pitch error

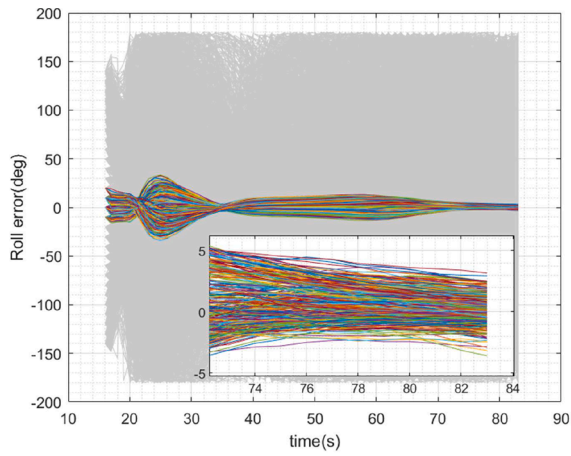


c) Yaw error

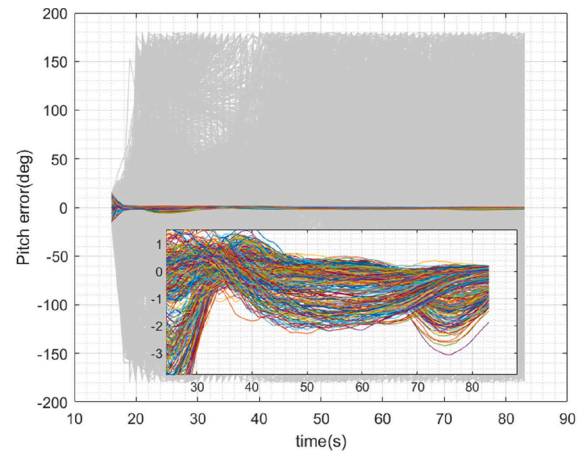
Fig. 15. Attitude errors of LG-KF over 3,509 simulations.

As is shown in Fig. 15, all results of the LG-KF algorithm converges in simulations. The roll angle error RMS is 0.475° , pitch angle RMS is 0.073° , and yaw angle RMS is 0.878° .

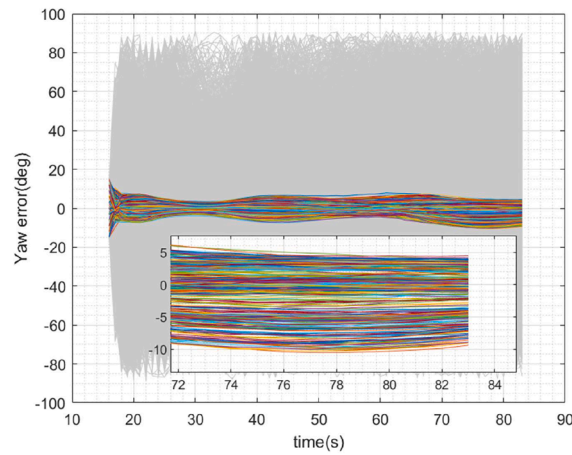
The results of the EKF algorithm are illustrated in Fig. 16.



a) Roll error



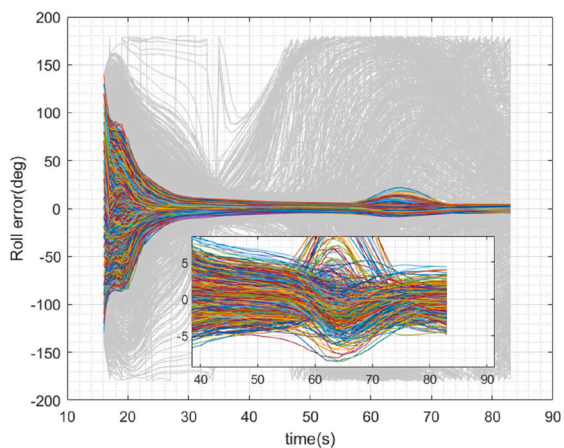
b) Pitch error



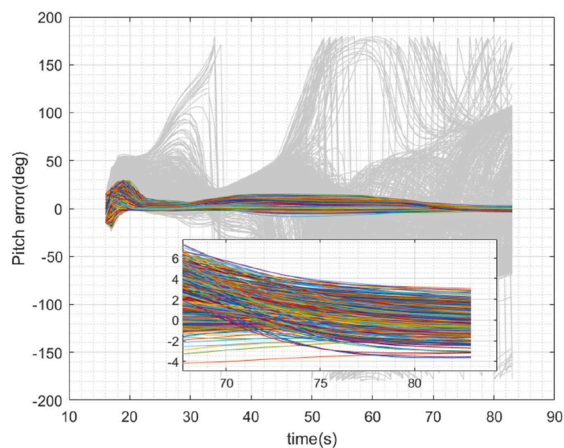
c) Yaw error

Fig. 16. Attitude error of EKF.

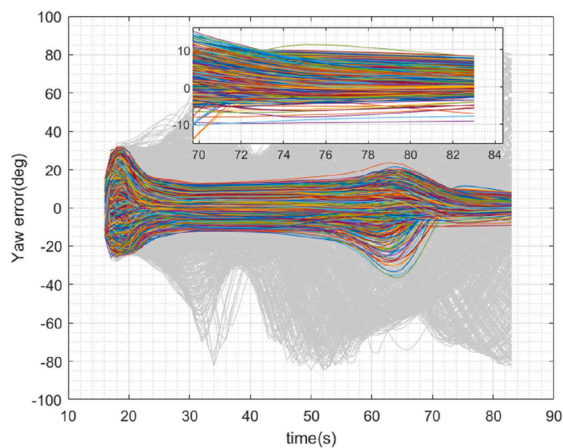
The EKF indicates a large number of divergent results under large initial misalignment angles, with only 518 results (14.8%) converging. The navigation accuracies of the converged results are as follows: yaw RMS: 3.679°, roll RMS: 1.313°, and pitch RMS: 0.531°. The results of the Quat-EKF algorithm are as Fig. 17:



a) Roll error



b) Pitch error

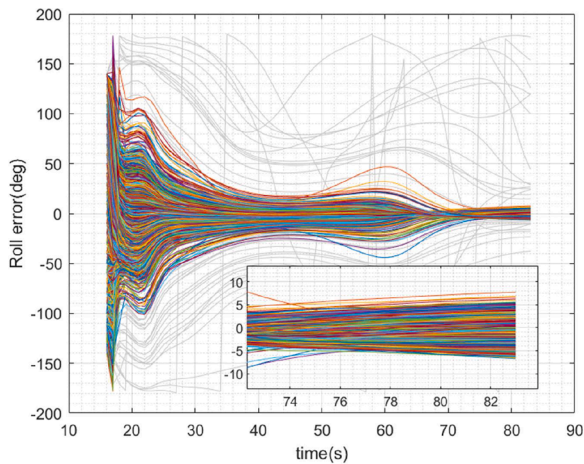


c) Yaw error

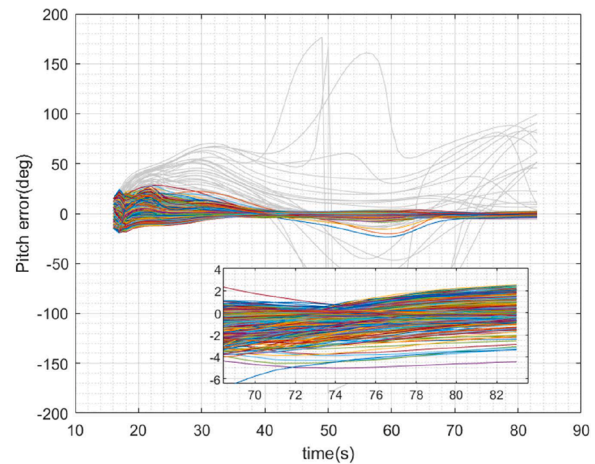
Fig. 17. Attitude error of Quat-EKF.

The Quat-EKF indicates fewer divergent results than the EKF, with 2,435 results (69.4%) converging. The navigation accuracies of the converged results are as follows: yaw RMS: 1.940°, roll RMS: 0.567°, and pitch RMS: 0.794°.

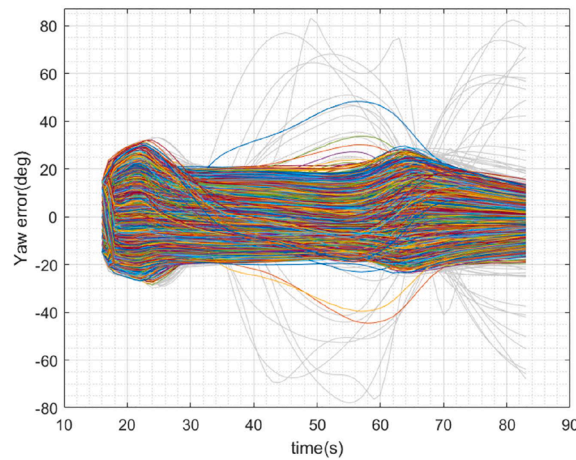
The simulation results using the ST-EKF algorithm are as Fig. 18:



a) Roll error over



b) Pitch error over



c) Yaw error over

Fig. 18. Attitude error of ST-EKF.

ST-EKF indicates a few divergent results. A total of 3576 out of 3,509 results (98.4%) converged, as indicated by the line in color in the graph. Navigation accuracies are as follows: yaw RMS: 6.061° , roll RMS: 2.516° , and pitch RMS: 0.592° .

Data availability

Data will be made available on request.

References

- [1] W.M. Ma, J.Y. Lu, YQ. Liu, Research progress of electromagnetic launch technology, *IEEE Transactions on Plasma Science* 47 (5) (May 2019) 2197–2205, <https://doi.org/10.1109/TPS.2019.2902416>.
- [2] S.X. Liu, Z.H. Lin, Y.C. Wang, et al., Three-body cooperative active defense guidance law with overload constraints: A small speed ratio perspective, *Chinese Journal of Aeronautics* 38 (2025) 103171, <https://doi.org/10.1016/j.cja.2024.08.002>.
- [3] L. Luo, Y.L. Huang, Z. Zhang, et al., A new Kalman filter-based in-motion initial alignment method for DVL-aided low-cost SINS, *IEEe Trans. Veh. Technol.* 70 (1) (2021) 331–343, <https://doi.org/10.1109/TVT.2020.3048730>.
- [4] J.W. Wang, Z.H. Deng, X.Y. Liang, et al., Functional iteration in-flight alignment method for projectiles MSINS, *IEEE/ASME Transactions on Mechatronics* 27 (5) (2022) 2887–2896, <https://doi.org/10.1109/TMECH.2021.3123951>.
- [5] S.Q. Li, X.Y. n Chen, Air alignment method of guided projectile based on INS/BDS, *Multimedia Technology and Enhanced Learning* 387 (2021), https://doi.org/10.1007/978-3-030-82562-1_42.
- [6] XL. Wang, Fast alignment and calibration algorithms for inertial navigation system, *Aerosp. Sci. Technol.* 13 (4-5) (2009) 204–209, <https://doi.org/10.1016/j.ast.2009.04.002>.
- [7] Z.H. Li, Y.H. Zhan, H.J. Du, et al., Robust adaptive SINS/CNS integrated navigation algorithm for Mars rovers with experimental verification, *Measurement* 236 (2024) 115087, <https://doi.org/10.1016/j.measurement.2024.115087>.
- [8] M.S. Wang, W.Q. Wu, P.Y. Zhou, et al., State transformation extended Kalman filter for GPS/SINS tightly coupled integration, *GPS Solution* 22 (2018) 112, <https://doi.org/10.1007/s10291-018-0773-3>.
- [9] W.T. Lu, X.L. Jia, Y.H. Teng, et al., Backward smoothing adaptive SVDCFKF integrated navigation algorithm, *Advances in Space Research* 74 (6) (2023) 2801–2813, <https://doi.org/10.1016/j.asr.2023.07.026>.
- [10] Y.L. Hao, Z.L. Xiong, Z.G. Hu, Particle filter for INS in-motion alignment, in: 2006 1ST IEEE Conference on Industrial Electronics and Applications, 2006, pp. 1–6, <https://doi.org/10.1109/ICIEA.2006.257150>. Singapore.
- [11] J. Mao, J.X. Lian, XP. Hu, Strapdown inertial navigation algorithms based on Lie group, *J. Navig.* 70 (1) (2017) 165–183, <https://doi.org/10.1017/S037346331600045X>.
- [12] A. Barrau, S. Bonnabel, Intrinsic filtering on Lie groups with applications to attitude estimation, *IEEe Trans. Automat. Contr.* 60 (2) (2015) 436–449, <https://doi.org/10.1109/TAC.2014.2342911>.
- [13] A. Barrau, Non-linear state error based extended Kalman filters with applications to navigation. *signal and image processing, Ecole Nationale Supérieure des Mines de Paris*, 2015.

- [14] L.B. Chang, Y.R. Luo, Log-linear error state model derivation without approximation for INS, *IEEE Transactions on Aerospace and Electronic Systems* 59 (2) (April 2023) 2029–2035, <https://doi.org/10.1109/TAES.2022.3197726>.
- [15] J. Tang, H.W. Bian, R.Y. Wang, et al., Lie group based nonlinear error models for SINS/DVL integrated navigation, *Ocean Engineering* 295 (2024) 116898, <https://doi.org/10.1016/j.oceaneng.2024.116898>.
- [16] B. Xu, Y. Guo, Y.P. Guo, et al., A SE(2)-based transfer alignment for large installation misalignment angle, *Measurement* 214 (2023) 112784, <https://doi.org/10.1016/j.measurement.2023.112784>.
- [17] K. Chen, Z.Y. Wang, Z.H. Fan, et al., Trajectory generator for hypersonic vehicle based on flight dynamics, *ICGNC*. Singapore, Springer, 845 (2022), https://doi.org/10.1007/978-981-19-6613-2_114.
- [18] K. Chen, F.Q. Shen, H.Y. Sun, J. Zhou, Hypersonic vehicle navigation algorithm in launch centered Earth-fixed frame, *Journal of Aeronautics* 40 (2019) 1212–1218 [Chinese].
- [19] K. Chen, J. Zhou, F.Q. Shen, et al., Hypersonic boost-glide vehicle strapdown inertial navigation system/global positioning system algorithm in a launch-centered earth-fixed frame, *Aerosp. Sci. Technol.* 98 (2020) 105679, <https://doi.org/10.1016/j.ast.2020.105679>.
- [20] K. Chen, S.S. Pei, F.Q. Shen, et al., Tightly coupled Integrated navigation algorithm for hypersonic boost-glide vehicles in the LCEF frame, *Aerospace* 8 (5) (2021) 124, <https://doi.org/10.3390/aerospace8050124>.
- [21] S.B. Liu, S.S. Pei, Z.Q. Ran, et al., Error-free strapdown inertial navigation system numerical updating algorithm in the launch-centered earth-fixed frame for hypersonic vehicles, *Aerosp. Sci. Technol.* 136 (2023) 108252, <https://doi.org/10.1016/j.ast.2023.108252>.
- [22] A. Barrau, Intrinsic filtering on SO(3) with discrete-time observations, in: 52nd IEEE Conference on Decision and Control, IEEE, Firenze, Italy, 2013, pp. 3255–3260, <https://doi.org/10.1109/CDC.2013.6760380>.